nature portfolio

https://doi.org/10.1038/s41565-021-00974-5

Supplementary information

Copper-catalysed exclusive CO_2 to pure formic acid conversion via single-atom alloying

In the format provided by the authors and unedited

Supplementary Materials for

Copper-catalyzed exclusive CO_2 to pure formic acid conversion *via* single-atom alloying

Tingting Zheng[1,2,3]†, Chunxiao Liu[1,3]†, Chenxi Guo[4]†, Menglu Zhang[3], Xu Li[3], Qiu Jiang[1], Weiqing Xue[3], Hongliang Li[3], Aowen Li[6], Chih-Wen Pao[5], Jianping Xiao[4*], Chuan Xia[1,2*], Jie Zeng[3*]

[1]School of Materials and Energy, University of Electronic Science and Technology of China, Chengdu 611731, P. R. China.

[2]Yangtze Delta Region Institute (Huzhou), University of Electronic Science and Technology of China, Huzhou, Zhejiang 313001, China.

[3]Hefei National Laboratory for Physical Sciences at the Microscale, Key Laboratory of Strongly-Coupled Quantum Matter Physics of Chinese Academy of Sciences, National Synchrotron Radiation Laboratory, Key Laboratory of Surface and Interface Chemistry and Energy Catalysis of Anhui Higher Education Institutes, Department of Chemical Physics, University of Science and Technology of China, Hefei, Anhui 230026, P. R. China.

[4]State Key Laboratory of Catalysis, Dalian Institute of Chemical Physics, Chinese Academy of Sciences, University of Chinese Academy of Sciences, Dalian National Laboratory for Clean Energy, Dalian 116023, P. R. China.

[5]National Synchrotron Radiation Research Center, Science-Based Industrial Park, Hsinchu 30076, Taiwan.

[6]School of Physical Sciences and CAS Key Laboratory of Vacuum Physics, University of Chinese Academy of Sciences, Beijing 100049, China.

*Corresponding author. E-mail: xiao@dicp.ac.cn (J.X.); chuan.xia@uestc.edu.cn (C.X.); zengj@ustc.edu.cn (J.Z.);

†These authors contributed equally to this work.

Computational methods

Density functional theory (DFT) calculations were performed using the Vienna *ab initio* simulation package (VASP)[1,2]. The revised Perdew-Burke-Ernzerhof (rPBE) functional[3] was used in all the calculations, where the cut-off energy was set to 400 eV, using the projector-augmented wave (PAW) method[4,5]. Cu(211) surface with 30 Cu atoms was constructed, and one of the Cu atom at the top layer of the surface was replaced by Pb, In or Bi, describing the structure of Pb_1Cu, In_1Cu, and Bi_1Cu, respectively (**Supplementary Fig. 33**). $M_1Cu(100)$ (p(3×3), 4 layers) and (111) (p(3×3), 4 layers) surfaces (M = Pb, In, Bi) were also built and studied as a comparison (**Supplementary Fig. 33**). A vacuum slab of 15 Å was applied for all the surface structures. All the structure optimizations were conducted with the force convergence less than 0.05 eV $Å^{-1}$. The Monkhorst-Pack k-point of 4×4×4 was applied for the optimization of Cu bulk, and a Monkhorst-Pack k-point of 3×3×1 was used for the optimizations of all surface structures. According to the adsorption structure of COOH* and HCOO* with two atoms bonded on the surface, two different adsorption conditions were studied for the adsorption of COOH* and HCOO*, including $M_1Cu_{M\text{-}Cu}$ (M = Pb, In, Bi; the adsorbate was bonded with Me site and Cu site on the surface, the Cu site is the first neighbor of M site) and $M_1Cu_{Cu\text{-}Cu}$ (M = Pb, In, Bi; the adsorbate was bonded with two Cu sites on the surface, one of the Cu site is the first neighbor of M site) (**Supplementary Fig. 33**). Different adsorbed states were also studied for CO* and H*, and adsorption energies with the most stable adsorbed states were applied to describe the catalytic performance on the surface.

Free energy corrections

The free energy corrections were applied on all the calculated energies at the temperature of 298 K. A standard thermodynamic correction was conducted, including the correction of the effect from zero-point energy, pressure, inner energy, and entropy[6]. The correction can be obtained following:

$$E_{cor} = E_{cor}^{ZPE} + E_{cor}^{U} + E_{cor}^{P} + E_{cor}^{S} \quad \text{(S1)}$$

where E_{cor}^{ZPE} presents the correction from the zero-point energy, E_{cor}^{U} and E_{cor}^{P} refer to the correction from inner energy and pressure, respectively. E_{cor}^{S} refers to the correction on entropy, where only vibrational motion was considered for adsorbates on the surface, while transilational, rotational and vibrational motions were all calculated for gas phase species (**Supplementary Table 5**).

Solvent effect corrections

The solvation effect on the adsorption energies were investigated due to the H-bond network in the reaction environment of electrocatalysis. A stablilzation of adsorption was reported for several adsorbates[7-9]. In this work, the solvation effect was investigated using an explicit model with 16 H_2O molecules were applied in one unit cell, establishing the water layer over 12 Å (**Supplementary Fig. 34**). A molecular dynamics (MD) simulation was performed first for 10000 steps with the timestep of 0.5 femtosecond over the bare $Pb_1Cu(211)$ surface. 5 snapshots were selected randomly from the MD simulation and the adsorption energies with explicit water in the system were calculated. The average of the calculated adsorption energies were performed as the one with solvation effect, where a stablilazation of 0.04, 0.18, and 0.06 eV were obateind for CO*, COOH*, and HCOO*. Less effect was found on adsorbed H*. Moreover, the solvation effect was also calculated using implicit models through VASPsol[10] calculations on $Pb_1Cu(211)$ surfaces, which are consistent with the calculations based on explicit models.

Reaction free energy calculations

The electrocatalytic carbon dioxide reduction reaction (CO_2RR) producing formic acid was studied in this work with also the consideration of the by-product of CO and the competitive process of hydrogen evolution reaction (HER). Accordingly, following elementary steps were estalished:

$CO_2 + (H^+ + e^-) + * \rightarrow COOH*$ **(R1)**

$CO_2 + (H^+ + e^-) + * \rightarrow HCOO*$ **(R2)**

$COOH* + (H^+ + e^-) \rightarrow HCOOH + *$ **(R3)**

$HCOO* + (H^+ + e^-) \rightarrow HCOOH + *$ **(R4)**

$COOH* + (H^+ + e^-) \rightarrow CO* + H_2O$ **(R5)**

$CO* \rightarrow CO + *$ **(R6)**

$(H^+ + e^-) + * \rightarrow H*$ **(R7)**

$(H^+ + e^-) + H* \rightarrow H_2 + *$ **(R8)**

All the gas phase free energies (G_{HCOOH}, G_{CO_2}) and adsorption free energies (G_{COOH*}, G_{HCOO*}, G_{CO*}, G_{H*}) were calculated referred to the gas phase free energies of CO, H_2 and H_2O. In addition, the chemical potential of a pair of $(H^+ + e^-)$ at 0 V vs. RHE ($G_{(H^+ + e^-)}$) can be referred to the 1/2 of chemical potential for H_2 molecule based on the computational hydrogen electrode (CHE) approximation[11]. Therefore, the reaction free energies can be calculated to be:

$$\Delta G_{R1} = G_{COOH*} - G_{(H^+ + e^-)} - G_{CO_2} \quad \text{(S2)}$$

$$\Delta G_{R2} = G_{HCOO*} - G_{(H^+ + e^-)} - G_{CO_2} \quad \text{(S3)}$$

$$\Delta G_{R3} = G_{HCOOH} - G_{(H^+ + e^-)} - G_{COOH*} \quad \text{(S4)}$$

$$\Delta G_{R4} = G_{HCOOH} - G_{(H^+ + e^-)} - G_{HCOO*} \quad \text{(S5)}$$

$$\Delta G_{R5} = G_{CO*} - G_{(H^+ + e^-)} - G_{COOH*} \quad \text{(S6)}$$

$$\Delta G_{R6} = -G_{CO*} \quad \text{(S7)}$$

$$\Delta G_{R7} = G_{H*} - G_{(H^+ + e^-)} \quad \text{(S8)}$$

$$\Delta G_{R8} = -G_{H*} - G_{(H^+ + e^-)} \quad \text{(S9)}$$

According to the CHE approximation, the potential dependent reaction energies for

electrochemical steps (**R1** – **R5**, **R7**, **R8**) can be calculated as:

$$\Delta G(U) = \Delta G(U_0) + e(U - U_0) \quad \text{(S10)}$$

where U and U_0 refer to the working electrode potential and the reference electrode potential at 0 V *vs.* RHE. Note that, the desorption of CO* in reaction **R6** was condiered to be potential independent.

The Reaction Phase Diagram (RPD)

A one-dimential RPD was established (**Fig. 4a**) based on the correlation of the adsorption free energies of COOH* and HCOO*. The globally optimal limiting (G_{RPD}-limiting) energies can be obtained at given descriptor, following:

$$G_{RPD} = min_i[max_j(\Delta G_{i,j})] \quad \text{(S11)}$$

where both mechanisms (denoted as *i* to describe COOH* path or HCOO* path) were constructed. The elementary steps with the highest energies in each given mechanism (denoted as *j* to describe **R1**/**R3** in COOH* path or **R2**/**R4** in HCOO* path) were compared to optimize the minimal G_{RPD}-limiting energies for CO_2RR. The four bold lines are the globally optimal limiting (G_{RPD}-limiting) energies, accounting for more favorable path via COOH* for strongly reactive catalysts (red lines, **Fig. 4a**), while the HCOO* path favors for relatively weak catalysts (blue lines, **Fig. 4a**). With the weakening of G_{ad} HCOO*, an increasing of the activity can be expected first within the studied range of the descriptor of -1.5 eV < G_{ad} HCOO* < 0.5 eV, where the total reaction was limited by the COOH* protonation with the descriptor stronger than -1.45 eV via COOH* path. An inhibition was obtained at a weaker G_{ad} HCOO* for the reaction activity, which is limited by the CO_2 protonation to COOH*. However, the HCOO* path shows more competitive when the HCOO* adsorption free energies were weaker than -0.83 eV, where a promotion of the activity can be expected due to the lower reaction energy of HCOO* protonation. With the further weakening of G_{ad} HCOO*, the whole activity was limited by the difficulty of CO_2 protonation to HCOO* (G_{ad} HCOO* > -0.29 eV).

Potential dependent activation barriers

A capacitor model was applied, performing the calculations of activation barriers for electrochemical steps at a constant electrode potential, namely, the scheme of 'charge-extrapolation'[12]. According to the capacitor model, the energy change between two states at a constant work function can be calculated following:

$$E_2(\varphi_1) - E_1(\varphi_1) = E_2(\varphi_2) - E_1(\varphi_1) + \frac{(q_2 - q_1)(\varphi_2 - \varphi_1)}{2} \quad \text{(S12)}$$

$$E_2(\varphi_2) - E_1(\varphi_2) = E_2(\varphi_2) - E_1(\varphi_1) - \frac{(q_2 - q_1)(\varphi_2 - \varphi_1)}{2} \quad \text{(S13)}$$

The scheme was further improved, obtaining the potential dependent barriers with only one round of calculations for initial, trantion and final states with an explicit model of water. Here, the transition states were located using the method of climbing image nudged elastic band (CI-NEB)[13], where the convergence of force were set to 0.1 eV/Å[14]. The strong correlations between the amount of electron transfer from the electrode to the water layer (Δq) and the relative work function of the system ($\Delta\Phi$) at initial, transition and final states reveal the reliability of the capacitor model in this system[7] (**Supplementary Fig. 41**). According to the capacitor model (Eq. S12 and S13), two pairs of data (barrier/reaction energy vs φ) can be obtained to build the linear relation describing extrapolated energy relevant to the change of relative work functions (**Supplementary Table 7**, **8**). Since the reaction free energy can be obtained following the CHE model at specific electrode potentials, the corresponding activation barrier can be located due to the extrapolated energies. As a result, the potential dependent activation energies can be calculated.

Microkinetic modeling

Full microkinetic modeling was applied for CO_2RR over the Pb_1Cu surface. The temperature of 298 K was applied with all the gas phase pressure (including P_{H^+}) set to 1.0[7,15,16]. All the studied elementary steps were performed together in the rate simulation, investigating either the optimal mechanisms for producing format acid or the selectivity of format acid, CO

and HER. The kinetic equations were applies as:

$$r_{R1} = P_{CO_2} \cdot P_{H^+} \cdot \theta_* \cdot k_{f1} - \theta_{COOH*} \cdot k_{b1} \quad \text{(S14)}$$

$$r_{R2} = P_{CO_2} \cdot P_{H^+} \cdot \theta_* \cdot k_{f2} - \theta_{HCOO*} \cdot k_{b2} \quad \text{(S15)}$$

$$r_{R3} = \theta_{COOH*} \cdot P_{H^+} \cdot k_{f3} - P_{HCOOH} \cdot \theta_* \cdot k_{b3} \quad \text{(S16)}$$

$$r_{R4} = \theta_{HCOO*} \cdot P_{H^+} \cdot k_{f4} - P_{HCOOH} \cdot \theta_* \cdot k_{b4} \quad \text{(S17)}$$

$$r_{R5} = \theta_{COOH*} \cdot P_{H^+} \cdot k_{f5} - P_{H_2O} \cdot \theta_{CO*} \cdot k_{b5} \quad \text{(S18)}$$

$$r_{R6} = \theta_{CO*} \cdot k_{f6} - P_{CO} \cdot \theta_* \cdot k_{b6} \quad \text{(S19)}$$

$$r_{R7} = P_{H^+} \cdot \theta_* \cdot k_{f7} - \theta_{H*} \cdot k_{b7} \quad \text{(S20)}$$

$$r_{R8} = P_{H^+} \cdot \theta_{H*} \cdot k_{f8} - P_{H_2} \cdot \theta_* \cdot k_{b8} \quad \text{(S21)}$$

where θ_{COOH*}, θ_{HCOO*}, θ_{CO*}, θ_{H*}, and θ_* refer to the surface coverage of COOH*, HCOO*, CO*, H* and free sites. The rate at steady state can be obtained with the condition of $\frac{d\theta}{dt} = 0$, shown in **Supplementary Table 9**.

Instrumentations

TEM images were taken on Hitachi H-7650 transmission electron microscope operating at an acceleration voltage of 100 kV. X-ray diffraction (XRD) patterns were recorded using a Philips X'Pert Pro Super diffractometer with Cu-K_α radiation (λ = 1.54178 Å). X-ray photoelectron spectroscopy (XPS) measurements were performed on a VG ESCALAB MK II X-ray photoelectron spectrometer with an exciting source of Al K_α = 1486.6 eV. The binding energies obtained in the XPS spectral analysis were corrected for specimen charging by referencing C 1s to 284.8 eV. HAADF-STEM images and energy-dispersive X-ray elemental mapping were carried out on JEOL ARM-200F field-emission transmission electron microscope operating at an accelerating voltage of 200 kV using Cu-based TEM grids. XAFS spectra of Cu *K*-edge and Pb L_3-edge were obtained at the 1W1B beam line of Beijing Synchrotron Radiation Facility operated at 2.5 GeV under 'top-up' mode with a constant current of 200 mA. The XAFS data were recorded under fluorescence mode with a 19-element Ge solid-state detector. The energy was calibrated according to the absorption edge of pure Cu and Pb foil, respectively. Part

of Pb L_3 and Bi L_3-edge XAFS spectra were obtained using beamline 44A of Taiwan Photon Source (TPS) at National Synchrotron Radiation Research Center, Taiwan. All data were collected in fluorescence mode using 7-element SDD detector and the incident photon energy were calibrated using standard Pb foil and Bi foil. Demeter software package was used to process the XAFS data. *In-situ* electrochemical attenuated total reflection Fourier-transform infrared spectroscopy (ATR-FTIR) experiments were conducted on a Thermo Scientific Nicolet iS50 FTIR spectrometer with silicon or ZnSe as the prismatic window at room temperature. *In-situ* Raman analysis were performed using a laser Raman analyzer LabRAM HR (Horiba/Jobin Yvon, Longjumeau) equipped with a frequency doubled Nd:YAG 785 nm laser.

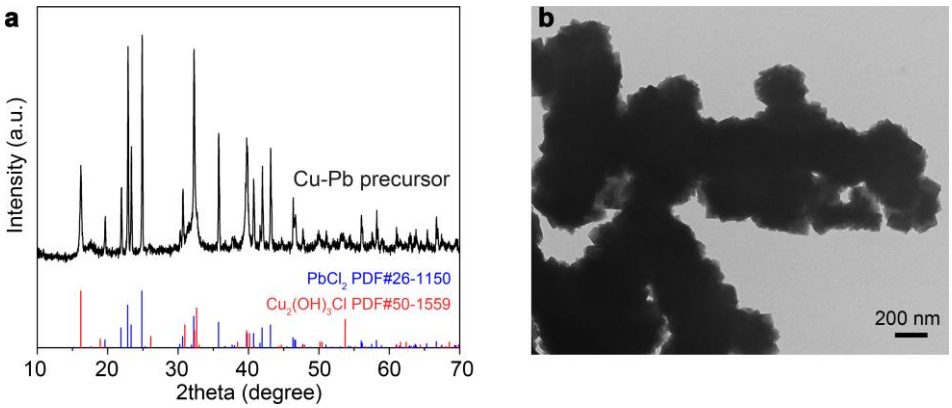

Supplementary Fig. 1 | Structural characterizations of Cu-Pb precursors. a, XRD pattern of as-prepared Cu-Pb precursor. The peaks were consistent with that of standard $PbCl_2$ and $Cu_2(OH)_3Cl$, indicating Cu-Pb precursor a hybrid structure of $PbCl_2$ and $Cu_2(OH)_3Cl$. **b**, TEM image of as-prepared Cu-Pb precursor with homogeneous morphologies.

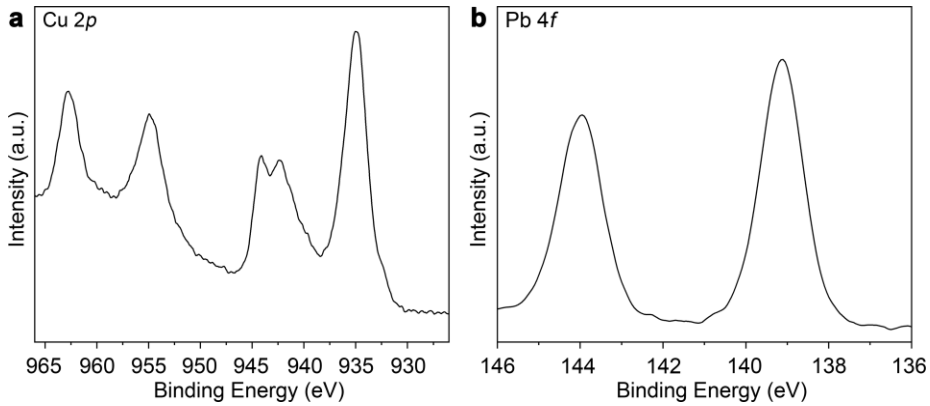

Supplementary Fig. 2 | XPS spectra of Cu-Pb precursors. a, Cu 2*p* spectrum of Cu-Pb precursor, the peaks were ascribed to a mixed valence states of surface Cu species. **b**, Pb 4*f* spectrum of Cu-Pb precursor, showing that the oxidation state of Pb is +2.

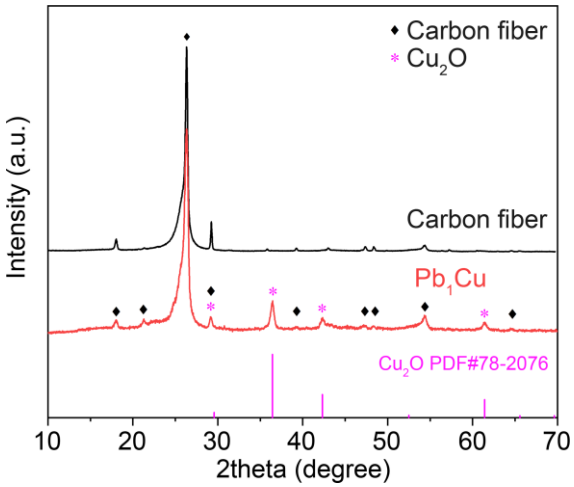

Supplementary Fig. 3 | XRD pattern of *in-situ* formed Pb_1Cu SAA catalyst on the GDL. The peaks of carbon fiber from GDL excluded, the spectrum is consistent with Cu_2O reference. This is due to electrochemical formed Cu matrix will be rapidly oxidized in Air during *ex-situ* XRD measurements. We speculated that the Pb_1Cu was formed *via* an electro-redeposition process of CuPb precursor ($PbCl_2/Cu_2(OH)_3Cl$ hybrids) under CO_2RR. Due to the higher electrode reduction potential, the dissolved Cu^{2+} was re-deposited onto the substrate prior to Pb^{2+}, with trace amount of Pb trapped on the lattice of Cu as single atoms. Such a conjecture was preliminarily testified by the ICP-AES test on the electrolyte where Cu-Pb precursors were *in-situ* reduced to Pb_1Cu, revealing that most of Pb was leached into the electrolyte, while only a small amount of Cu was detected. The concentration of Pb in the as-formed Pb_1Cu was determined to be about 7.9 wt.% and 4.4 wt.%, according to XPS and ICP-AES, respectively, indicating that Pb was probably enriched on the surface of Pb_1Cu. Deeper insight into the formation mechanism requires extra efforts on *operando* techniques, which will be explored in our following works.

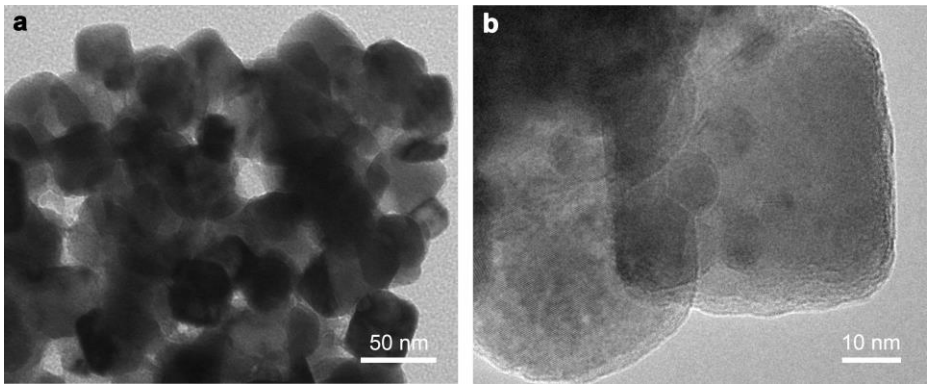

Supplementary Fig. 4 | TEM images of Pb_1Cu SAA catalyst with low- and high-magnification. The images showed that the morphologies of sample turned into nanocube during surface reconstruction over *in-situ* electroreduction.

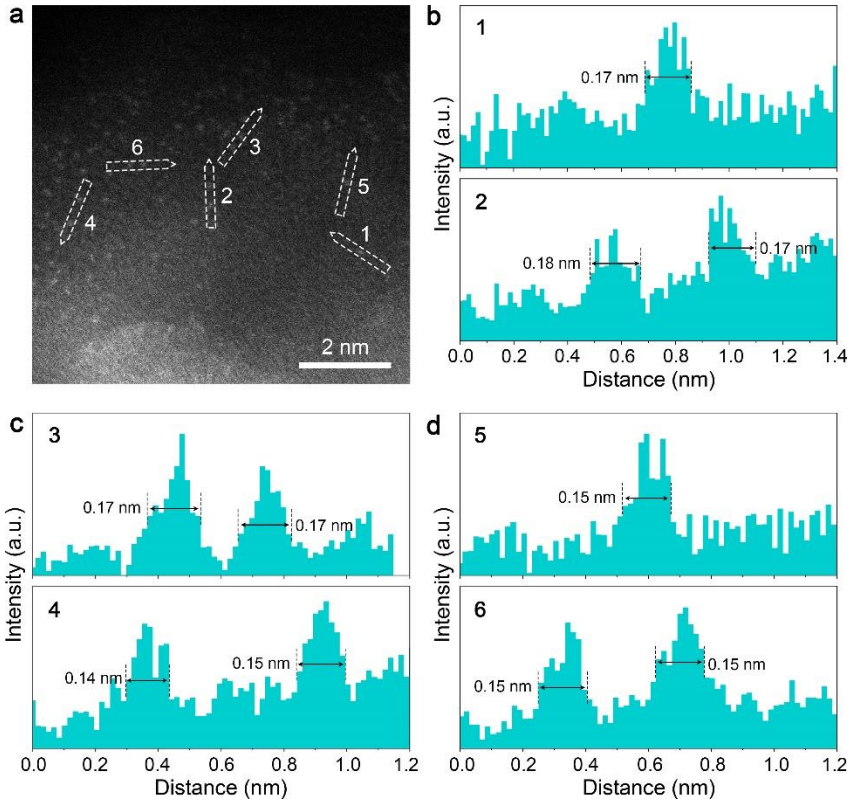

Supplementary Fig. 5 | Histogram of spot intensities of Pb_1Cu SAA in Fig. 1b.

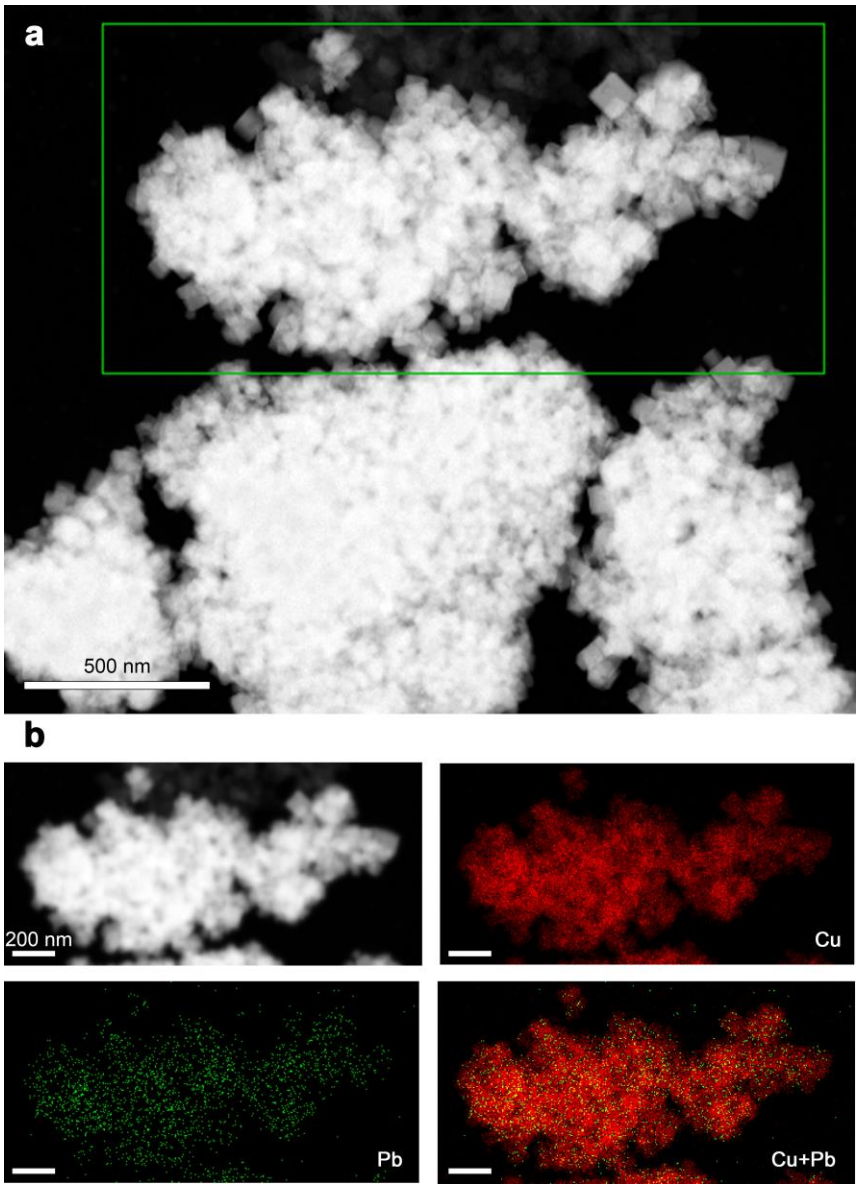

Supplementary Fig. 6 | STEM-EDS mapping of Pb_1Cu SAA catalyst at large scale. The mapping results exhibited that Cu as well as Pb were evenly distributed at micrometer level, with no Pb particle or cluster existed.

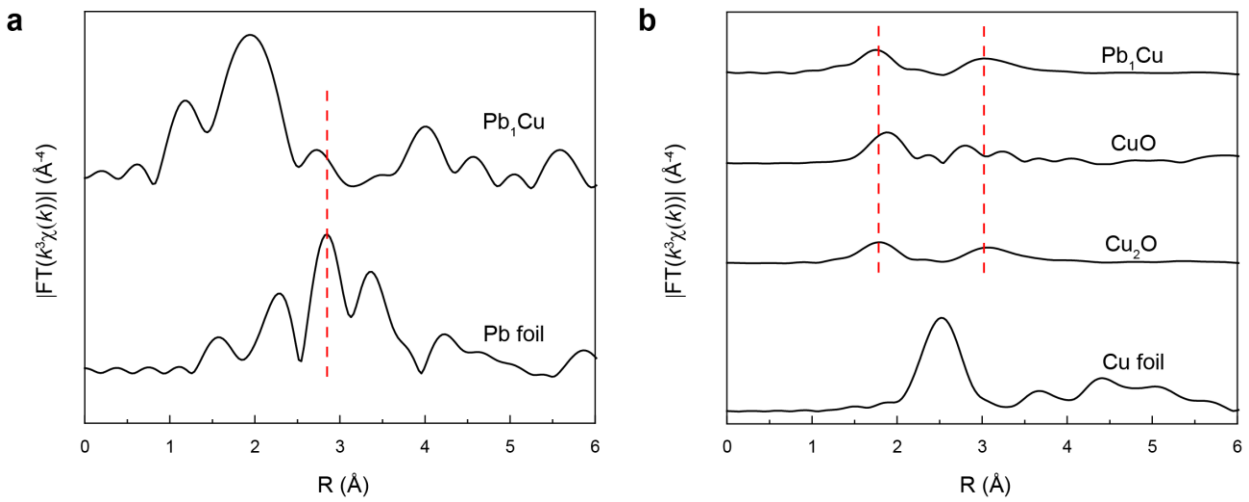

Supplementary Fig. 7 | *Ex-situ* EXAFS spectra of Pb_1Cu. a, *Ex*-situ EXAFS spectra at Pb L_3-edge of Pb_1Cu catalyst with Pb foil as reference. **b,** *Ex*-situ EXAFS spectra at Cu *K*-edge of Pb_1Cu catalyst. Cu, CuO and Cu_2O were used for references. The EXAFS spectra of Pb_1Cu indicate the formation of Cu_2O due to the oxidation by air, which is consistent with XRD results (**Supplementary Fig. 3**).

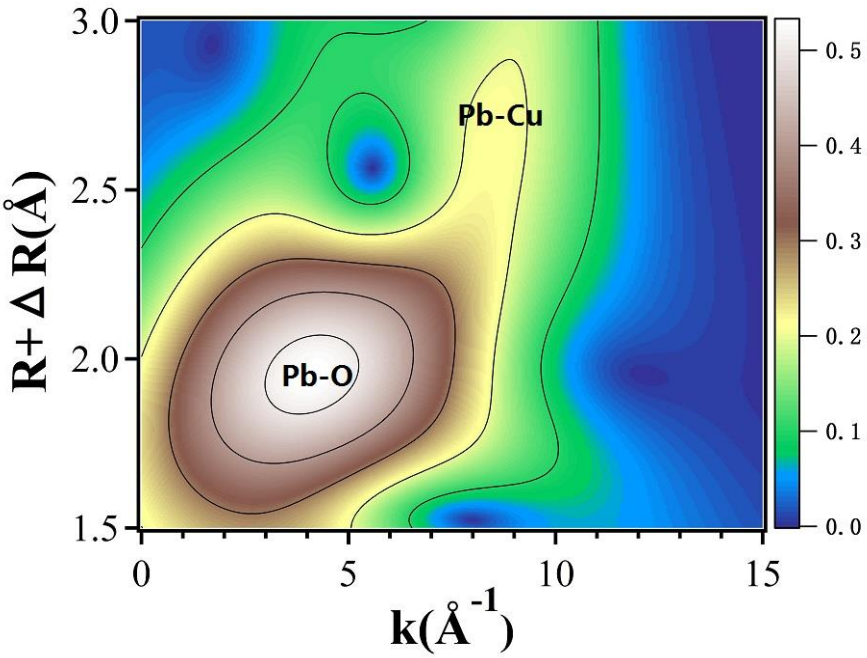

Supplementary Fig. 8 | XAFS wavelet transforms (WT) for the Pb_1Cu catalyst. The *Y*-axis of the WT plots shows the radical distance and the *X*-axis reflects the *k*-space resolution of the backscattering atom. It can be obviously observed both the Pb-O bond and Pb-Cu bond, verifying the formation of Pb single atoms in Cu matrix. Zhong *et al.* pointed out that "EXAFS is not sensitive enough to identify single atoms in many cases, which may easily confuse the contributions from small clusters or nanoparticles due to the polydispersity and disorder effects. Also, HAADF-STEM measures very limited regions, which may easily miss other compositions." *[Appl. Phys. Lett. 2020, 116, 191903]*. Thus, besides the EXAFS analysis, we have screened a lot of regions of Pb_1Cu by HAADF-STEM and did not observe any cluster and particle. Moreover, we have employed XRD analysis along with large-scale EDS-mapping to preclude the presence of Pb agglomerations (**Supplementary Fig. 3** and **6**). Therefore, we believe with a high certainty that Pb atom was mono-dispersed across Cu.

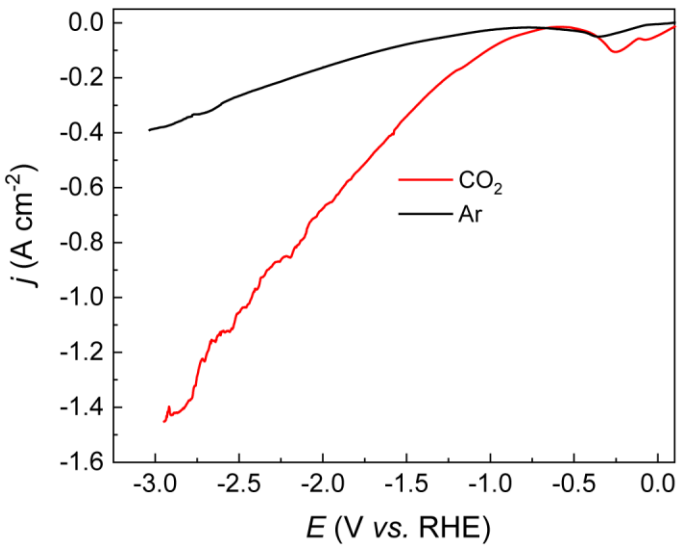

Supplementary Fig. 9 | LSV of Pb_1Cu SAA catalyst. The polarized curves were collected in a conventional three-electrode flow-cell system using a scan rate of 0.01 V s^{-1}. 1 mL min^{-1} 0.5 M $KHCO_3$ electrolyte and 50 sccm CO_2 or Ar flow were provided. The values of potential were presented without *iR* compensation.

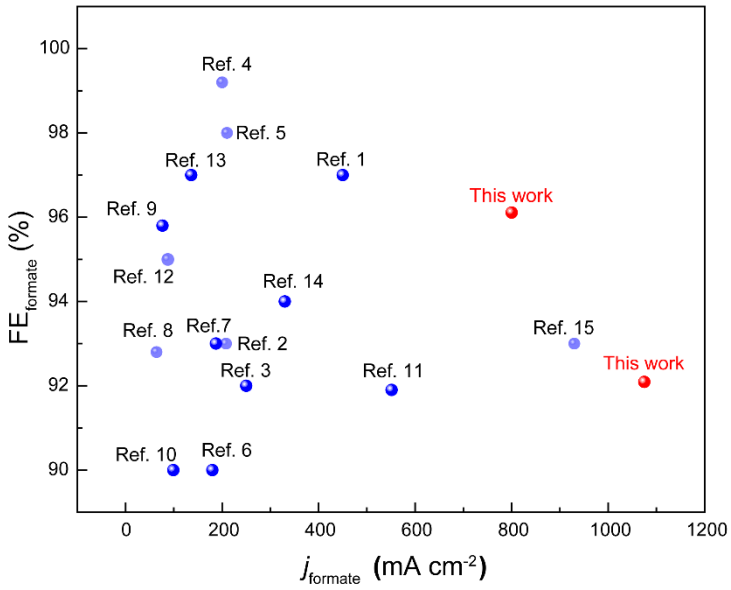

Supplementary Fig. 10 | Performance metrics of different CO_2RR formate generation catalysts in flow cell. The translucent ball represents the catalyst performed in KOH electrolyte. *[Ref. 1: Nat. Commun.* ***11****, 3633 (2020)]; [Ref. 2: Angew. Chem. Int. Ed.* ***59****, 10807-10813 (2020)]; [Ref: 3: Adv. Sci. doi.org/10.1002/advs.201902989]; [Ref. 4: Angew. Chem. Int. Ed.* ***132****, 15124-15130 (2020)]; [Ref. 5: Nat. Commun.* ***10****, 2807 (2019)]; [Ref. 6: Adv. Mater.* ***30****, 1802858 (2018)]; [Ref. 7: Angew. Chem. Int. Ed.* ***130****, 16346-16351 (2018)]; [Ref. 8: J. Mater. Chem. A* ***6****, 10313 (2018)]; [Ref. 9: Adv. Mater.* ***32****, 2002822 (2020)]; [Ref. 10: J. Appl. Electrochem.* ***49****, 917-928 (2019)]; [Ref. 11: Chem. Commun.* ***57****, 1502-1505 (2021)]; [Ref. 12: Nat. Energy* ***4****, 776-785 (2019)]; [Ref. 13: Nat. Commun.* ***10****, 2807 (2019)]; [Ref.14: J. CO_2 Util.* ***42****, 101287(2020)]; [Ref. 15: ACS Energy Lett.* ***6****, 1, 79-84 (2021)].*

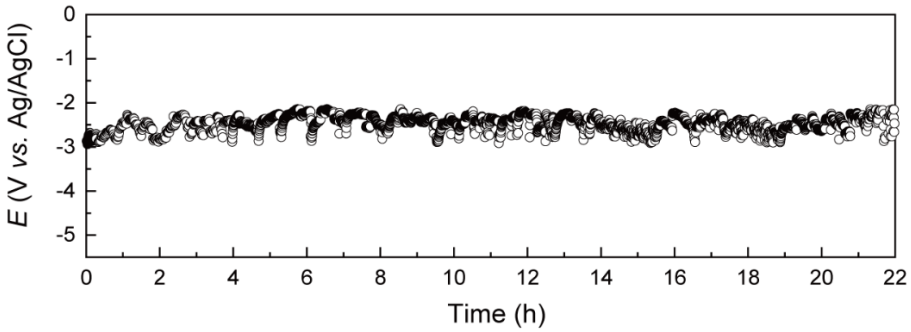

Supplementary Fig. 11 | The stability test data corresponded to Fig. 2c without *iR*-compensation. In our flow cell stability test, several factors might account for the fluctuations of the operational potentials. First, the evolved gas bubble on the catalyst surface at large current density could interfere with the overall impedance of cell and thus, in turn, affect the applied potentials. Although the gas products selectivity is not that appreciable, however, due to the applied large current density of 500 mA cm^{-2}, the generation rate of gas products could be up to 2.6 μmol cm^{-1} s^{-1}, that is about 64 μL cm^{-1} s^{-1}, which was significantly enough to disturb the triple-phase interface and thus affect the impedance of the cell. Second, during our stability test, the outlet gas products were directly vented into an on-line GC (Shimadzu GC-2014) for real-time analysis. However, the switch of valve of GC during the automatic sampling will cause a sharp change in the gas pressure of cathode chamber, resulting in a violent fluctuation in the potential. In addition, for the long-term stability test, once in a while we have to flow DI water to the gas channels to wash off the carbonate deposits on the back of GDE, which will inevitably exert disturbance on the potential.

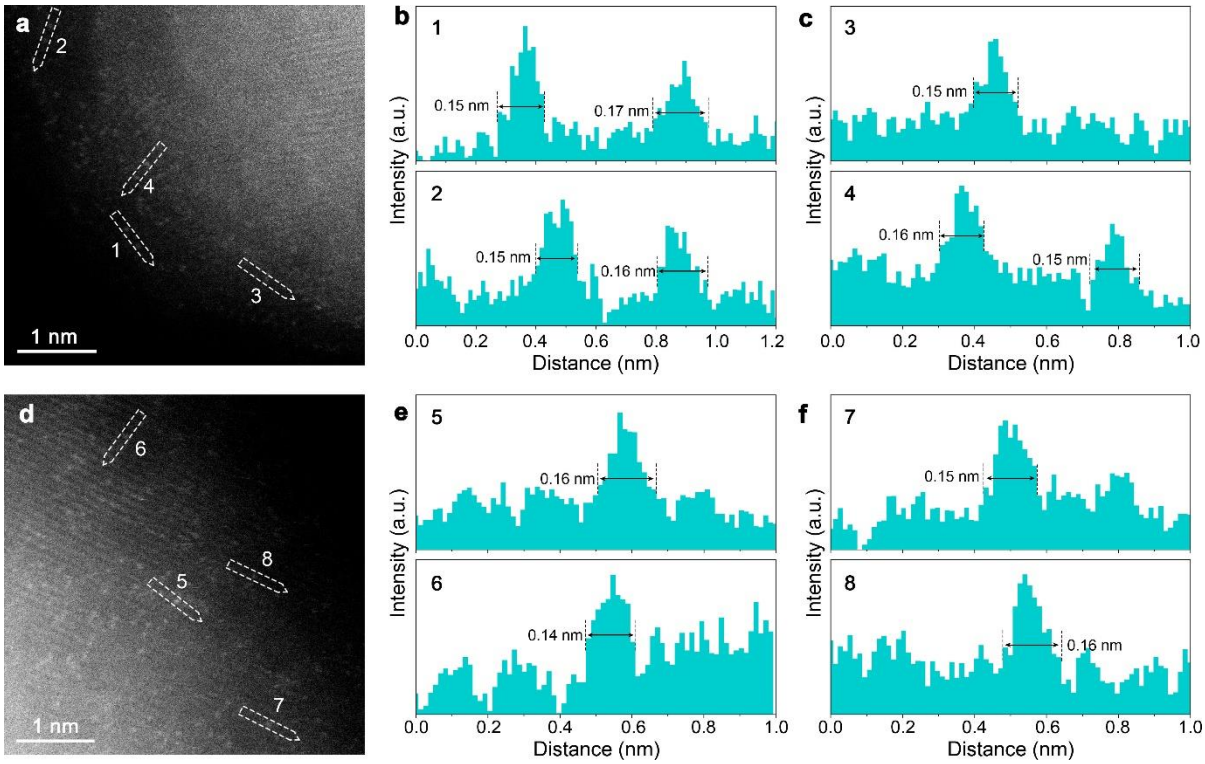

Supplementary Fig. 12 | Post-catalysis HAADF-STEM images along with histogram of spot intensities for Pb_1Cu SAA. The Pb single atoms were still mono-dispersed among Cu matrix after the stability test.

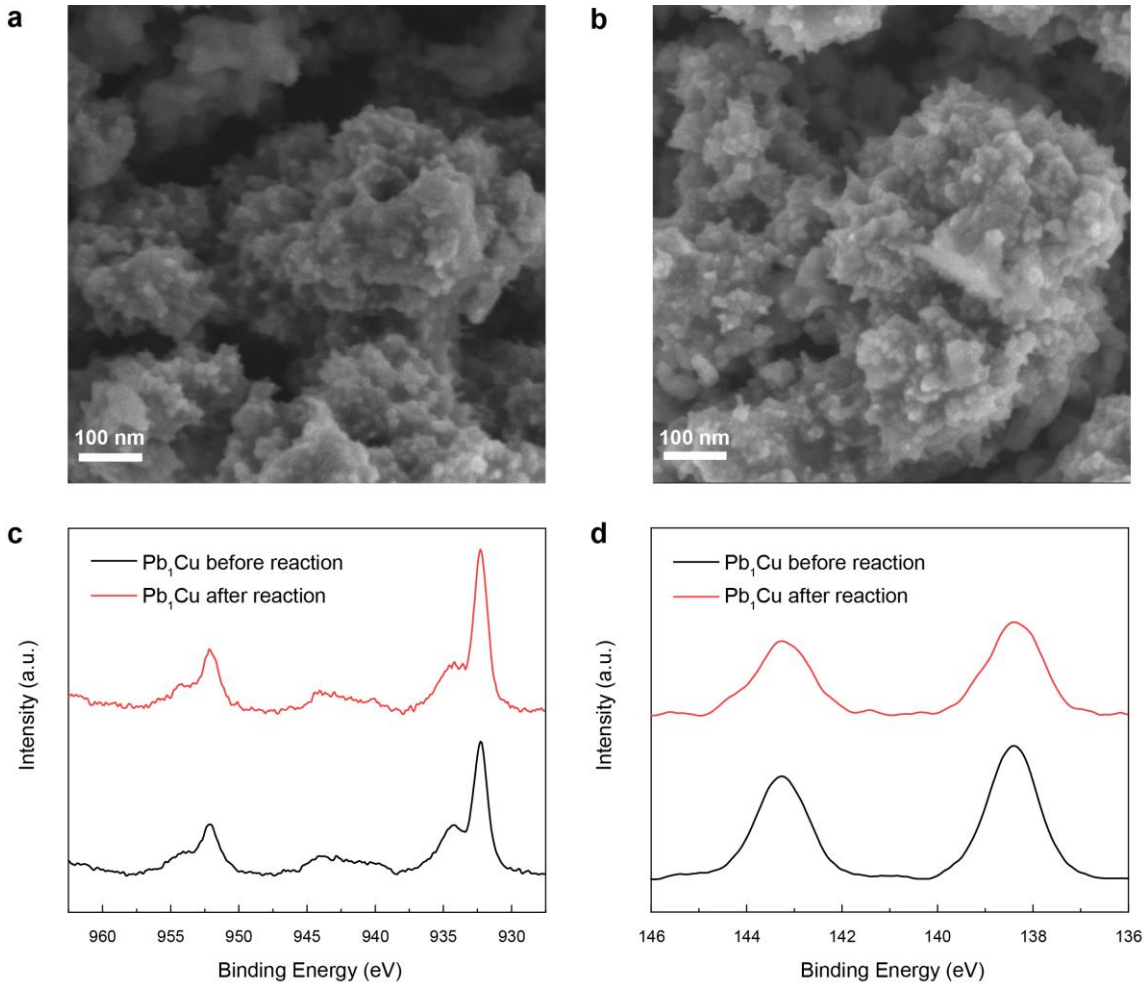

Supplementary Fig. 13 | SEM and XPS characterizations of Pb_1Cu SAAs before and after long-term electrolysis. a,b, SEM images of Pb_1Cu SAAs before (**a**) and after electrolysis (**b**). **c,d,** Cu 2*p* spectra (**c**) and Pb 4*f* spectra (**d**) of fresh Pb_1Cu and the one after electrolysis. From the SEM image, it seems that the particle underwent a mild change in morphology after long-term electrolysis, which does not impact greatly on the overall performance.

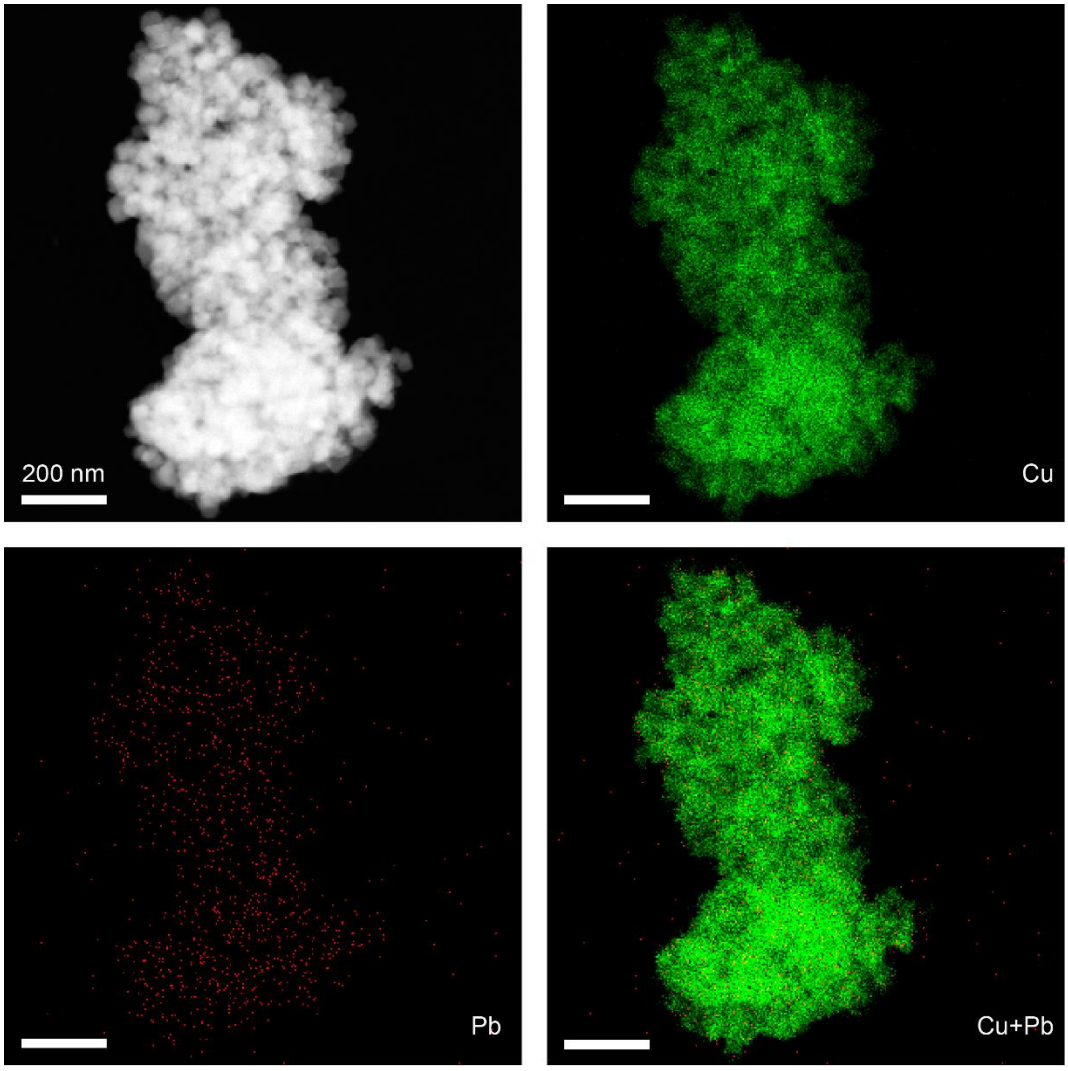

Supplementary Fig. 14 | STEM-EDS mapping of Pb_1Cu SAA after long-term electrolysis.

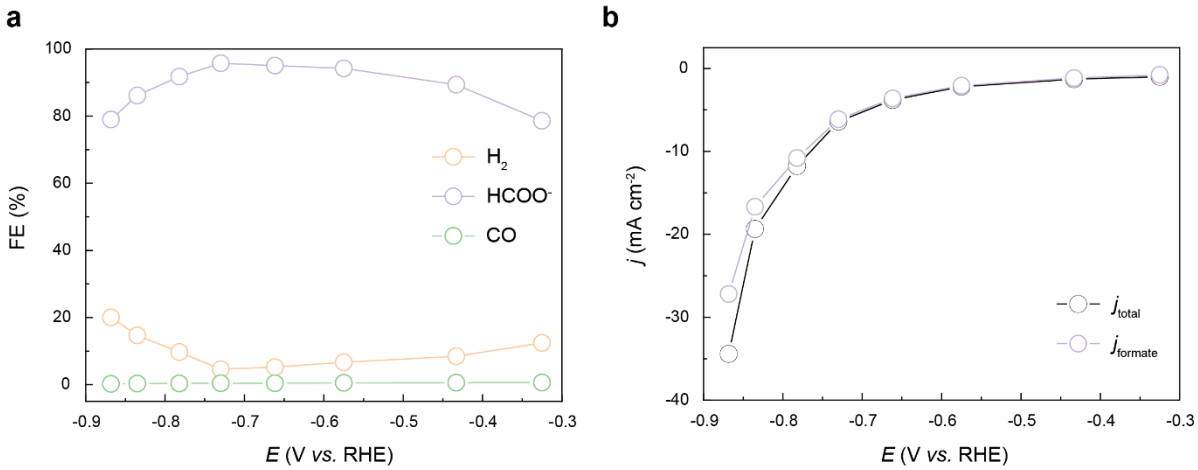

Supplementary Fig. 15 | CO_2RR performance of Pb_1Cu catalyst in a H-cell. a,b, FEs of H_2, CO and $HCOO^-$ (a) and the corresponding current densities (b) of Pb_1Cu in a H-cell. The inhabitation of CO_2 mass transportation in H-cell resulted in a limited current density and lower selectivity at lager overpotential due to competitive HER. In addition, the carbon paper substrate that was first operated at large current density in flow cell was further subjected to the electrified polarization in electrolyte of H-Cell, which might cause the impairment of the hydrophobicity on the back side of GDE and render the occurring of HER at higher potential.

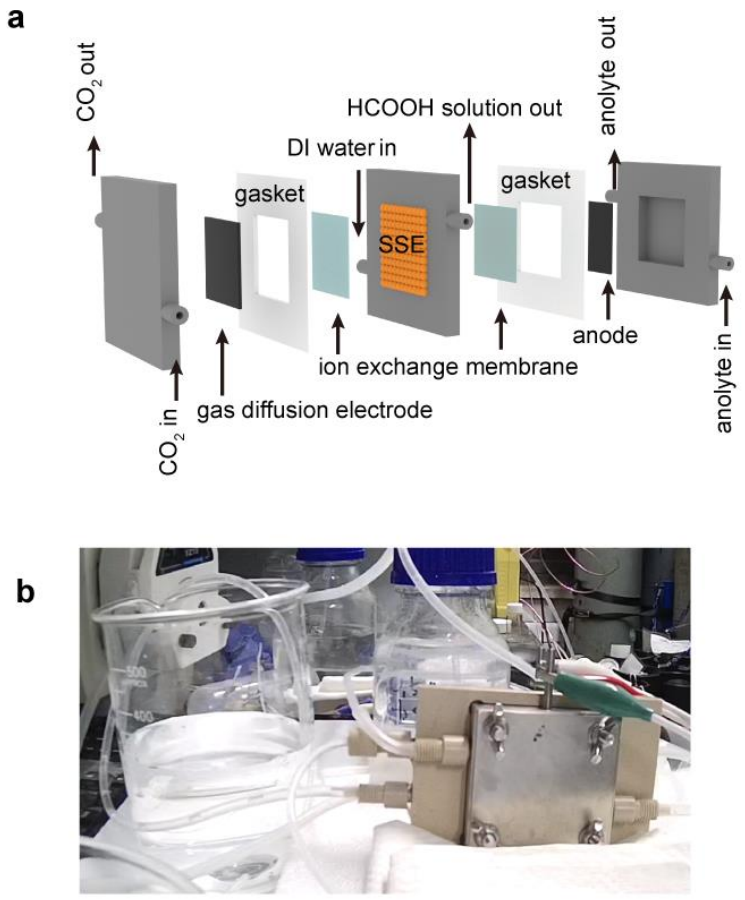

Supplementary Fig. 16 | Schematic and digital image of MEA-SSE electrolyzer for pure HCOOH production. When CO_2 is reduced, the generated anion $HCOO^-$ driven by the electrical field travels through the AEM towards the middle solid-electrolyte channel. At the same time, protons generated by water oxidation on the anode side can move across the CEM to compensate the charge. For the adopted SSE is a proton conductor, the HCOOH product could be formed via the ionic recombination of crossed ions at the interface between the middle channel and AEM, and diffuse away through the liquid DI water.

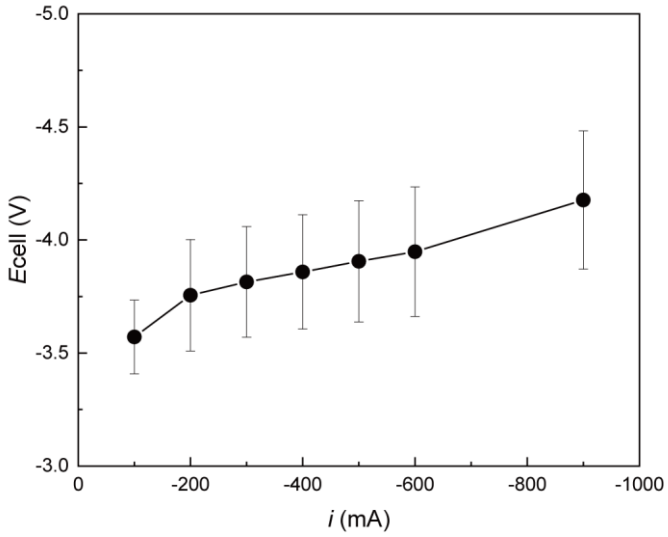

Supplementary Fig. 17 | I-V curve collected during MEA-SSE electrolysis over Pb_1Cu SAA catalyst for pure HCOOH production. The values of cell voltage were manually compensated according to the measured cell resistance. The error bars correspond to the standard deviation of three independent measurements.

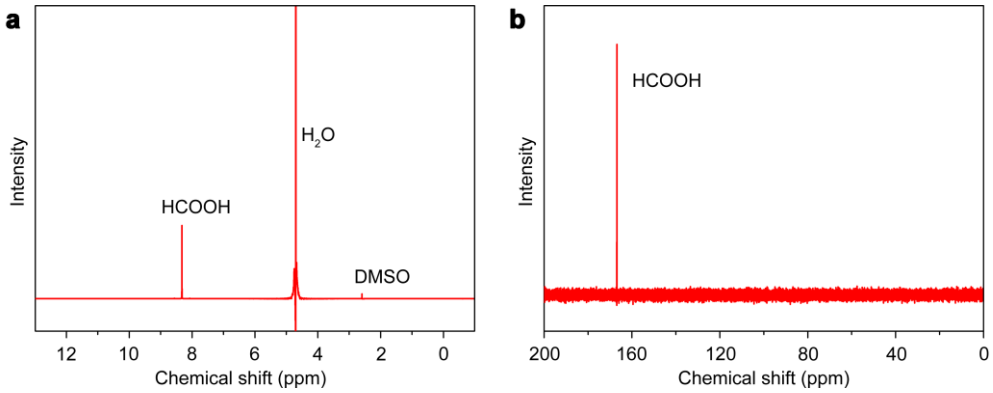

Supplementary Fig. 18 | NMR spectra. a,**b**, Typical ^{1}H (**a**) and ^{13}C (**b**) NMR spectra for as-prepared pure HCOOH solution from electrocatalytic CO_2 reduction, proving that no other liquid products are formed.

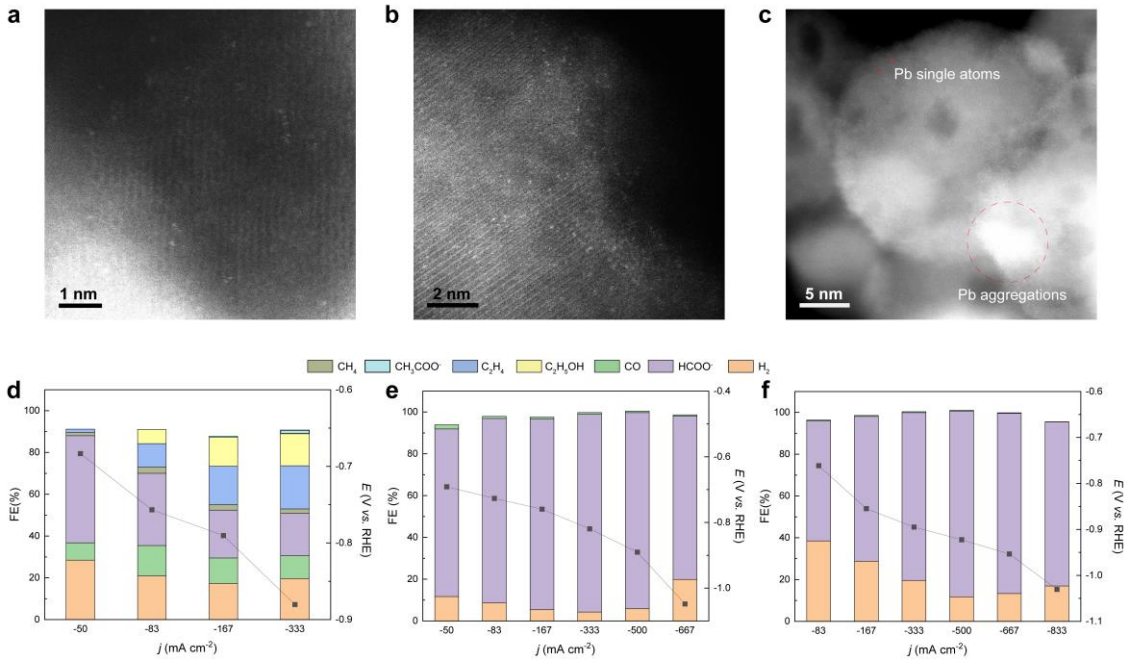

Supplementary Fig. 19 | Study of the effect of Pb content of Pb_1Cu on the CO_2RR performance. a,b,c, HAADF-STEM images of Pb_1Cu (SS) catalyst **(a),** Pb_1Cu (S) catalyst **(b),** and Pb_1Cu (L) catalyst **(c). d,e,f,** CO_2RR performance of Pb_1Cu (SS) catalyst **(d)**, Pb_1Cu (S) catalyst **(e)**, and Pb_1Cu (L) catalyst **(f)** in a flow cell. Pb_1Cu (SS), Pb_1Cu (S) and Pb_1Cu (L) were prepared in a similar manner to Pb_1Cu except that the amount of Pb precursors changed to12 mg, 38 mg and 300 mg, respectively. The Pb concentrations of Pb_1Cu (SS), Pb_1Cu (S) and Pb_1Cu (L) were calculated to be 0.7 wt.%, 2.5 wt.%, and 23.0 wt.%, respectively by ICP-AES. From HAADF-TEM images, we observed that the Pb single atoms of Pb_1Cu (SS) was notably sparser than those of Pb_1Cu (S) and Pb_1Cu, while Pb single atoms and Pb aggregations co-existed in Pb_1Cu (L). The three samples were then tested for CO_2RR in a flow cell. For Pb_1Cu (SS), we found that formate was the major product at 50 mA cm^{-2}, while multiple C_1 and C_2 products could be observed at higher current density. We presumed that this is due to the limited Pb single atoms were unable to activate the whole surface Cu atoms, resulting in the competitive reactions to other C_1 and C_2 products. When the amount of Pb precursors increased, we find that the selectivity of Pb_1Cu (S) still remained above 90% at 500 mA cm^{-2}. However, further increasing current density leads to the drastic drop of selectivity below 80%, likely due to the inadequate density of Pb single atoms. For the Pb_1Cu sample, synthesizing with 115 mg Pb precursor, we achieved above 90% formate FE even at 1000 mA cm^{-2} (**Fig. 2a**), demonstrating the critical role of the density of isolated Pb atoms. However, in terms of Pb_1Cu (L), we can see that formate is still the exclusive CO_2RR products, but its selectivity is much inferior to that of Pb_1Cu due to the formation of Pb aggregations. Thus, we inferred that isolated Pb atoms play the key role on modifying nearby Cu, but in a limited range. If the density of Pb atoms is too small, large portion of Cu could not be activated, resulting in the competitive reaction to produce other products. Moreover, a certain amount of Pb atoms is required to sustain formate formation at high current density.

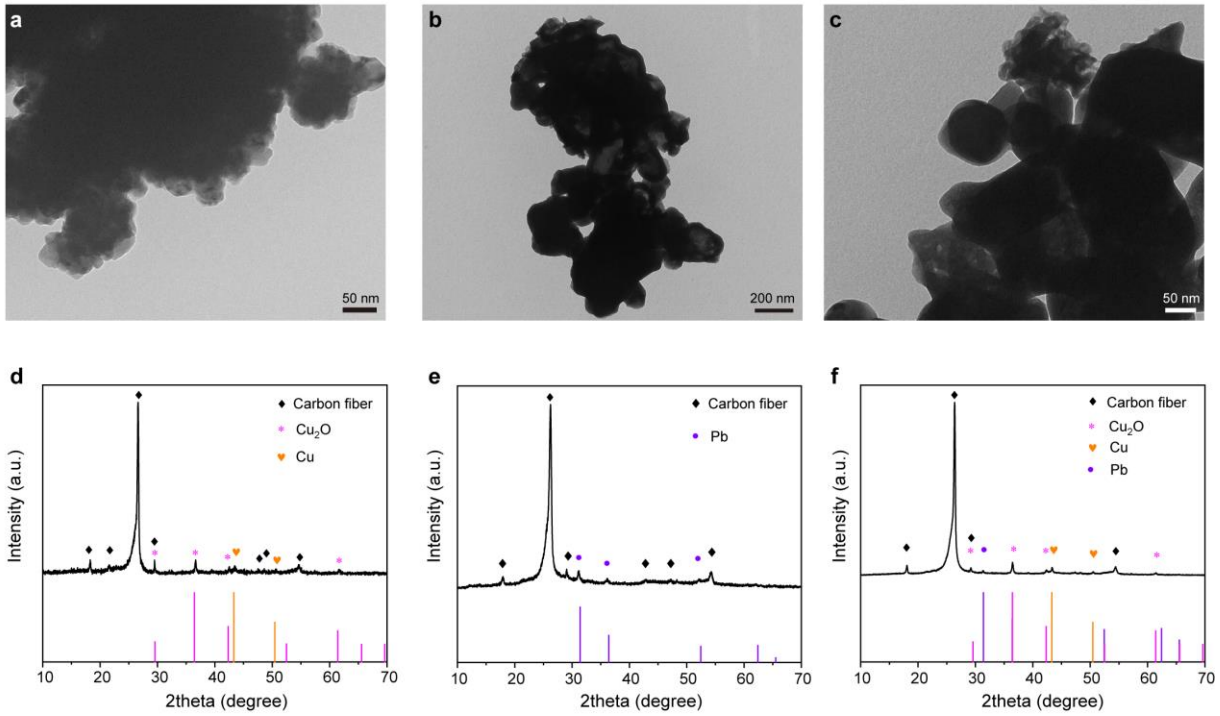

Supplementary Fig. 20 | Structural characterizations of as-prepared Cu, Pb, and Pb@Cu nanoparticle. a-c, The TEM images showed Cu (**a**), Pb (**b**), and Pb@Cu (**c**) nanoparticles with a uniform size distribution were obtained. **d-f**, XRD patterns confirm the composition of samples. With slight oxidation when exposed to air, the peaks of corresponding oxide could be found.

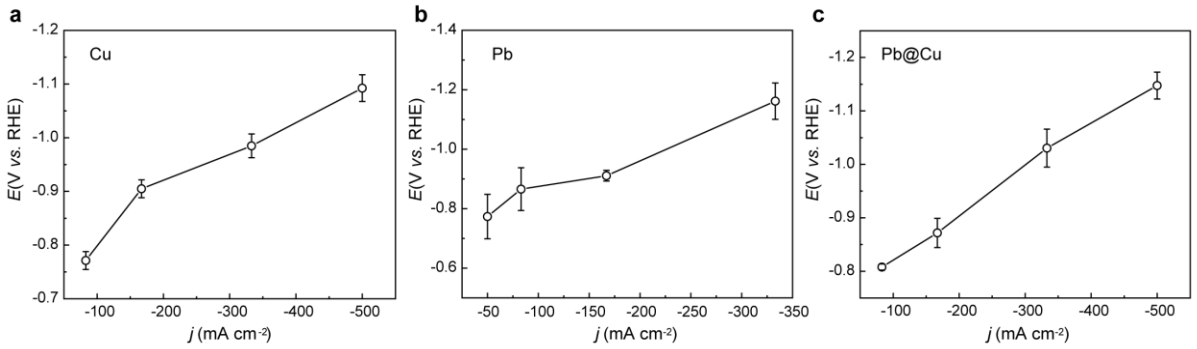

Supplementary Fig. 21 | I-V curve collected during flow-cell electrolysis over Cu (a), Pb (b), and Pb@Cu (c) catalysts for CO_2 reduction. The test was conducted under the same conditions as that of Pb_1Cu SAA catalyst. It reveals that pure Pb sample exhibited a large overpotential and sluggish kinetic towards CO_2 conversion. The values of potential were manually compensated according to the measured electrolyte resistance and corrected to RHE scale.

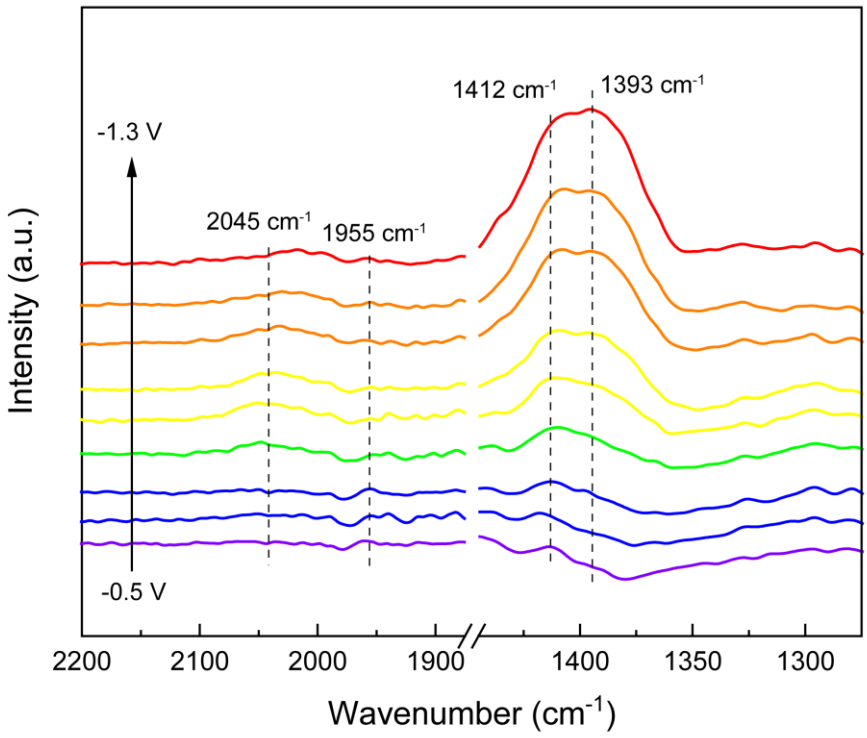

Supplementary Fig. 22 | *In-situ* ATR-FTIRS recorded at different applied potentials for Pb@Cu. Two infrared bands appeared at 1955 and 2045 cm^{-1}, which were ascribed to the surface-bounded CO on Cu. In addition, a broad infrared band of $HCOO^-$ with two peaks was detected at 1393 cm^{-1} and 1412 cm^{-1} over Pb@Cu, indicating $HCOO^-$ was adsorbed on Cu and Pb, respectively.

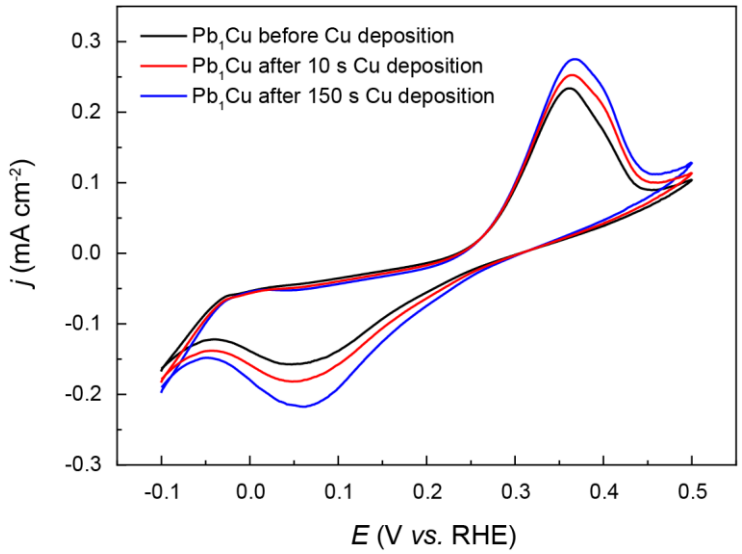

Supplementary Fig. 23 | Study of cyclic voltammetry (CV) before and after electro-deposition of Cu layer with different thickness on Pb_1Cu SAAs. The electro-deposition was carried out in Ar bubbled 0.05 M H_2SO_4 containing 5 mM $CuSO_4$ at 0.05 V *vs.* RHE for 10 s and 150 s, respectively. From the CV curves, we did not observe the oxidation of peak of Pb for Pb_1Cu, ruling out the existence of Pb particles. Moreover, the oxidation peak of Cu became broader after electro-deposition, suggesting the successful deposition of Cu layers.

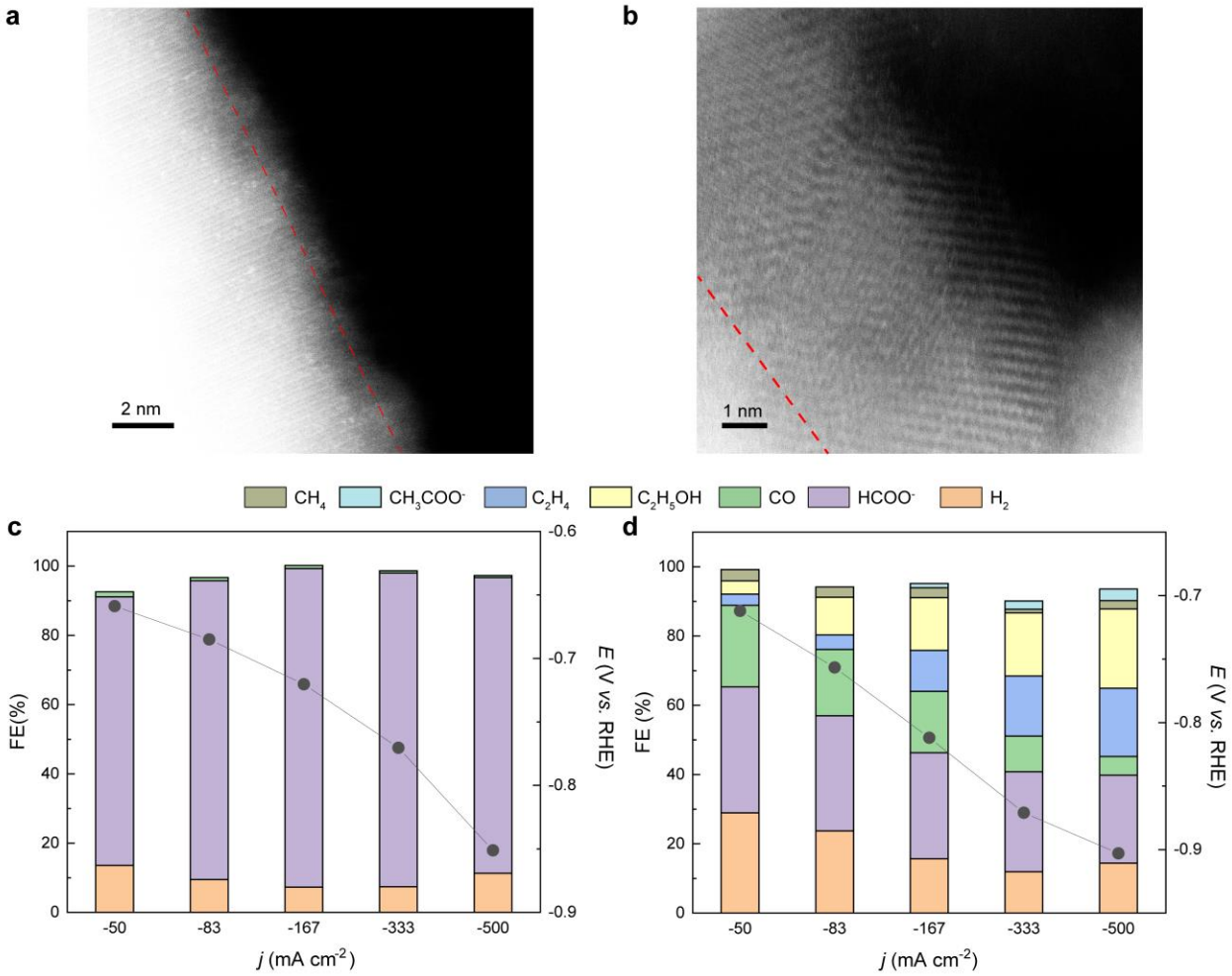

Supplementary Fig. 24 | Study of the electro-deposition of Cu layer with different thickness on Pb_1Cu SAAs. a-d, HAADF-STEM images of Pb_1Cu deposited with a thin Cu layer (**a**) and thick layer (**b**). CO_2RR performances of Pb_1Cu deposited with a thin Cu layer (**c**) and a thick Cu layer (**d**). The electro-deposition was carried out in Ar bubbled 0.05 M H_2SO_4 containing 5 mM $CuSO_4$ at 0.05 V *vs.* RHE for 10s and 150s, respectively. From HAADF-STEM images, we observe an ultrathin layer of less than 1 nm was formed on Pb_1Cu after 10s deposition. Increasing the deposition time to 150s results in a thick layer of more than 5 nm of Cu on Pb_1Cu, where the bright spot of Pb single atoms were significantly covered. We found that the Pb_1Cu deposited with an ultrathin-layer Cu still produce formate as the exclusive product for CO_2RR. In stark contrast, Pb_1Cu deposited with a thick Cu layer generates multiple C_1 and C_2 products. In general, when covered by a thin-layer Cu, the isolated Pb could still activate the surface Cu, and thus regulate the CO_2RR reaction pathway towards formate. However, such an effect was blocked when a thick Cu layer was deposited. This phenomenon implies that the isolated Pb atoms in Pb_1Cu SAA may not be the intrinsically active sites but more likely behave as a modifier to activate the neighboring Cu sites.

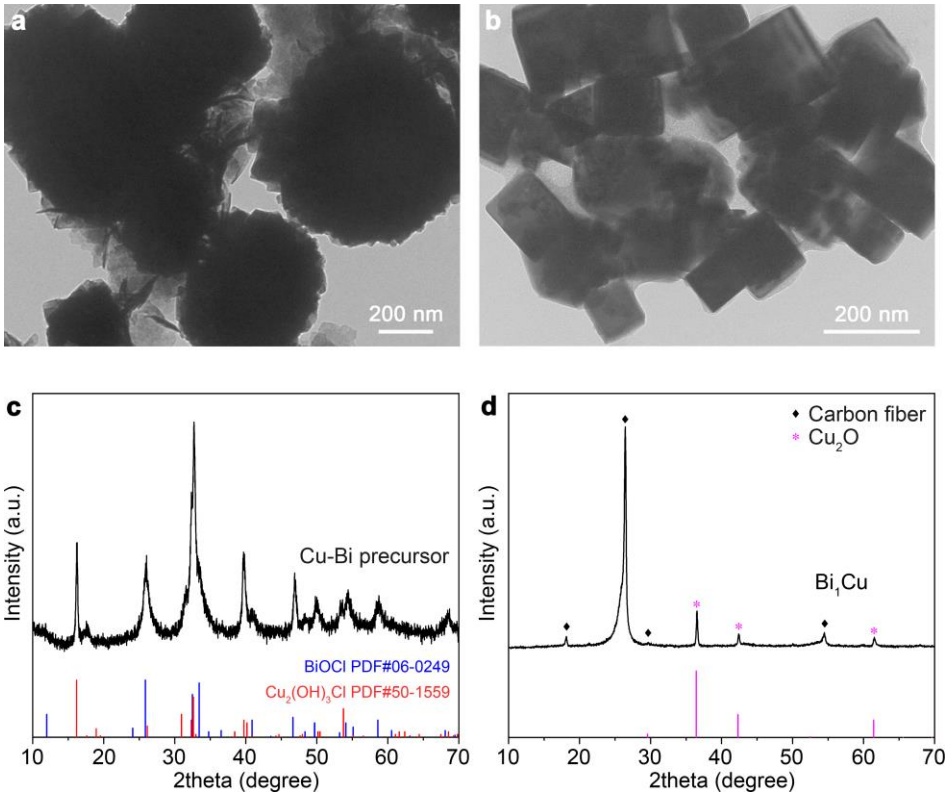

Supplementary Fig. 25 | Structural characterizations of Cu-Bi precursors and Bi_1Cu SAA catalyst. a-d, After *in-situ* electroreduction, the shape of Cu-Bi transformed from irregular nanohybrids (**a**) into nanocubes (**b**). XRD pattern (**c**) of Cu-Bi precursors was measured, showing its composition of $Cu_2(OH)_3Cl$ and BiOCl. However, only Cu_2O phase was detected after reduction (**d**), suggesting the formation of mono-dispersed Bi.

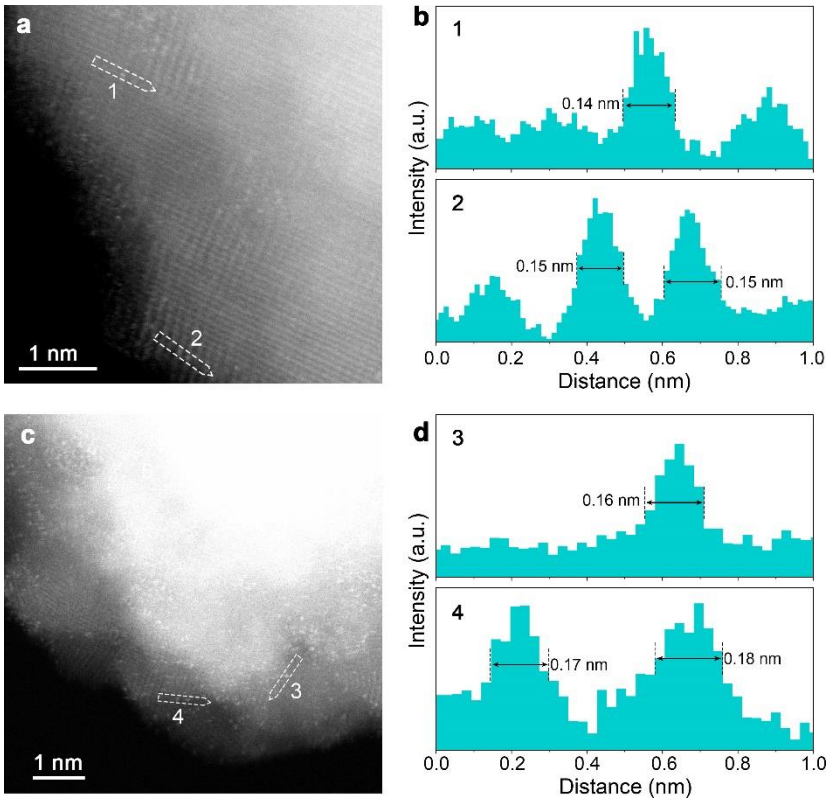

Supplementary Fig. 26 | HAADF-STEM images and histogram of spot intensities of Bi_1Cu SAA catalyst. The Bi single atoms were mono-dispersed among Cu matrix.

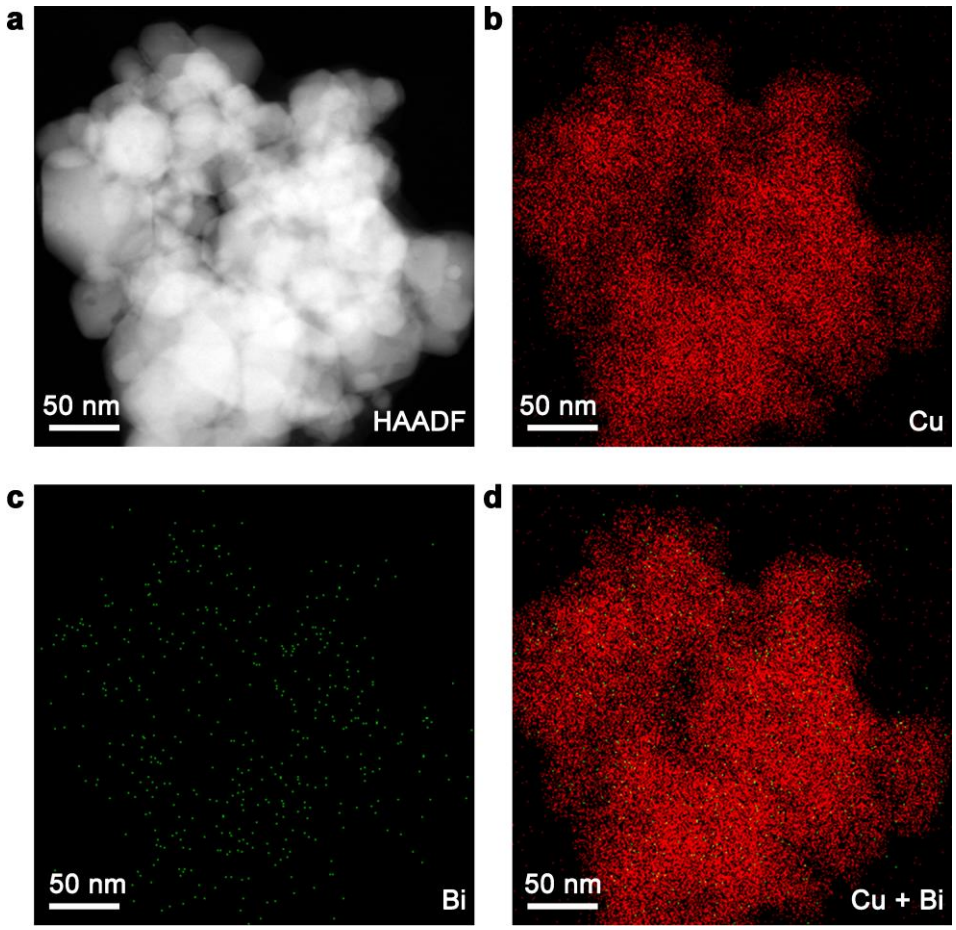

Supplementary Fig. 27 | STEM-EDS mapping of Bi_1Cu SAA catalyst. The images showed the atomic dispersion of Bi in the Cu matrix.

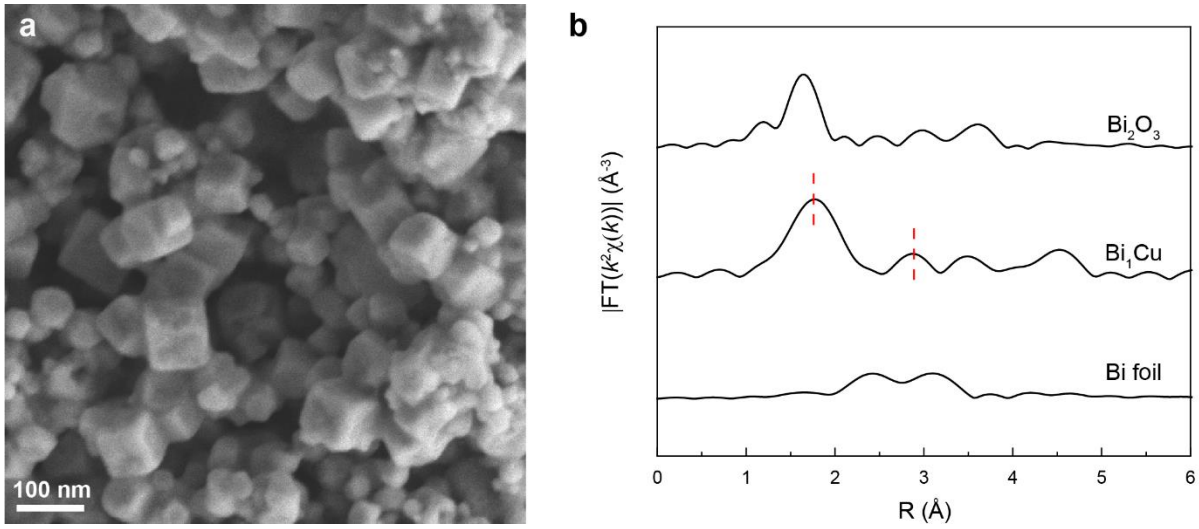

Supplementary Fig. 28 | SEM images and *ex-situ* EXAFS spectra at Bi L_3-edge of Bi_1Cu catalyst. EXAFS spectra of Bi L_3-edge exhibits two peaks around 1.77 and 2.89 Å attributed to Bi-O and Bi-Cu bonds, respectively, indicating the atomically dispersed Bi atoms in Cu.

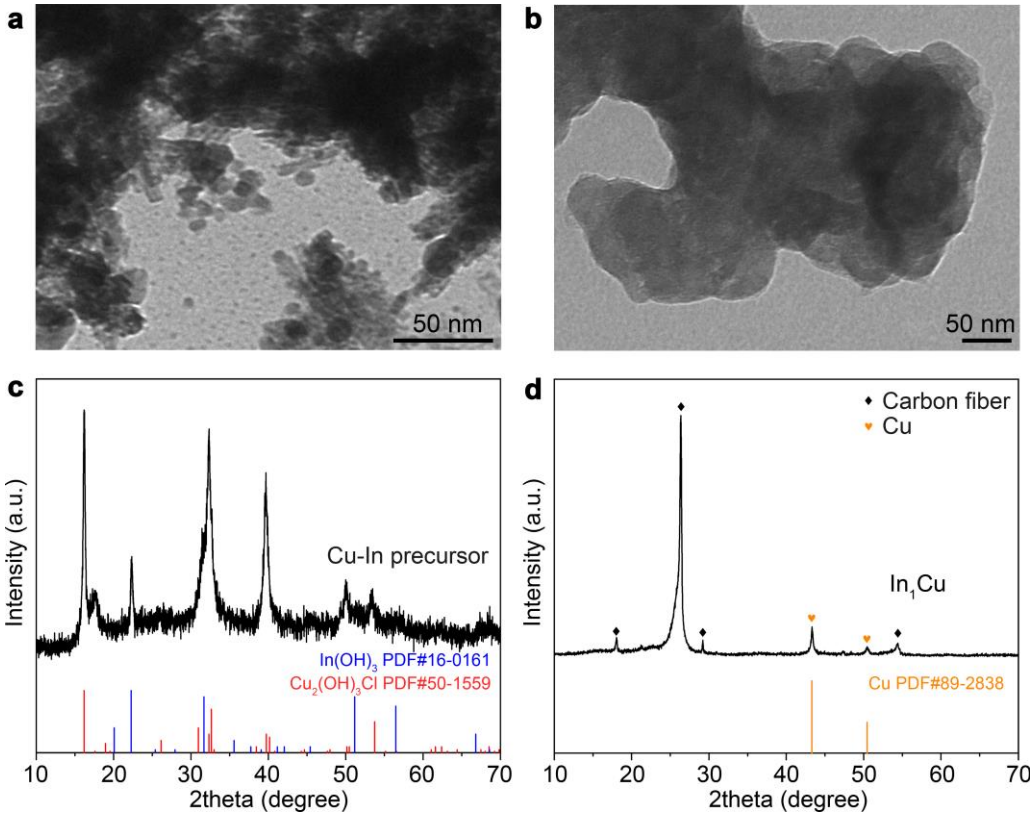

Supplementary Fig. 29 | Structural characterizations of Cu-In precursors and In_1Cu SAA catalyst. a-d, TEM images of Cu-In precursors before (**a**) and after (**b**) *in-situ* electroreduction. XRD pattern (**c**) of Cu-In precursors, revealing its composition of $Cu_2(OH)_3Cl$ and $In(OH)_3$. Similarly, only Cu_2O phase was observed after electrochemical reduction (**d**).

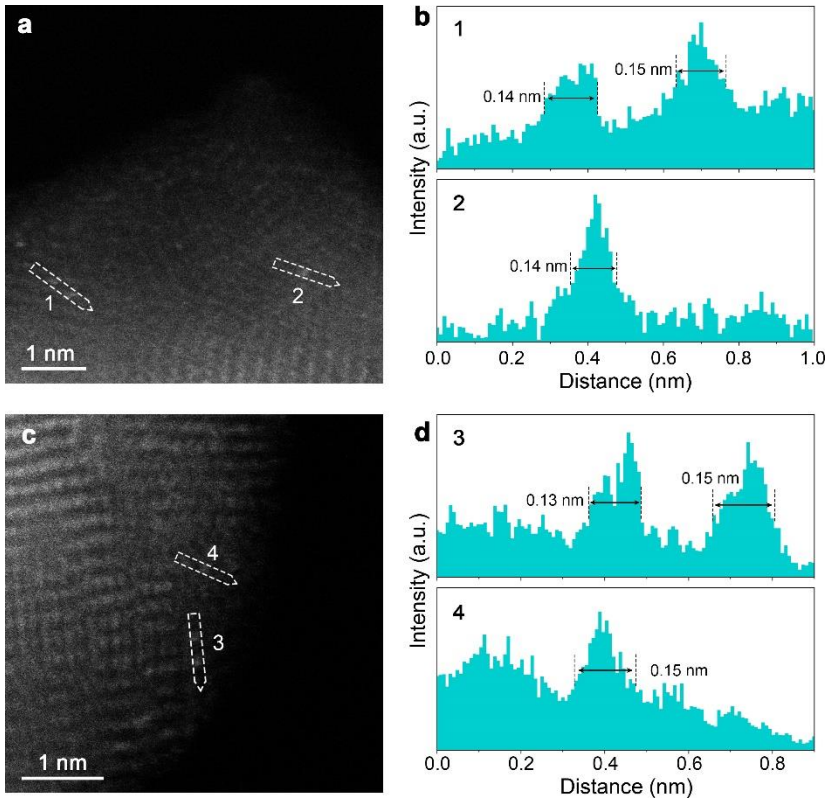

Supplementary Fig. 30 | HAADF-STEM images and histogram of spot intensities of In_1Cu SAA catalyst. The In single atoms were mono-dispersed among Cu matrix.

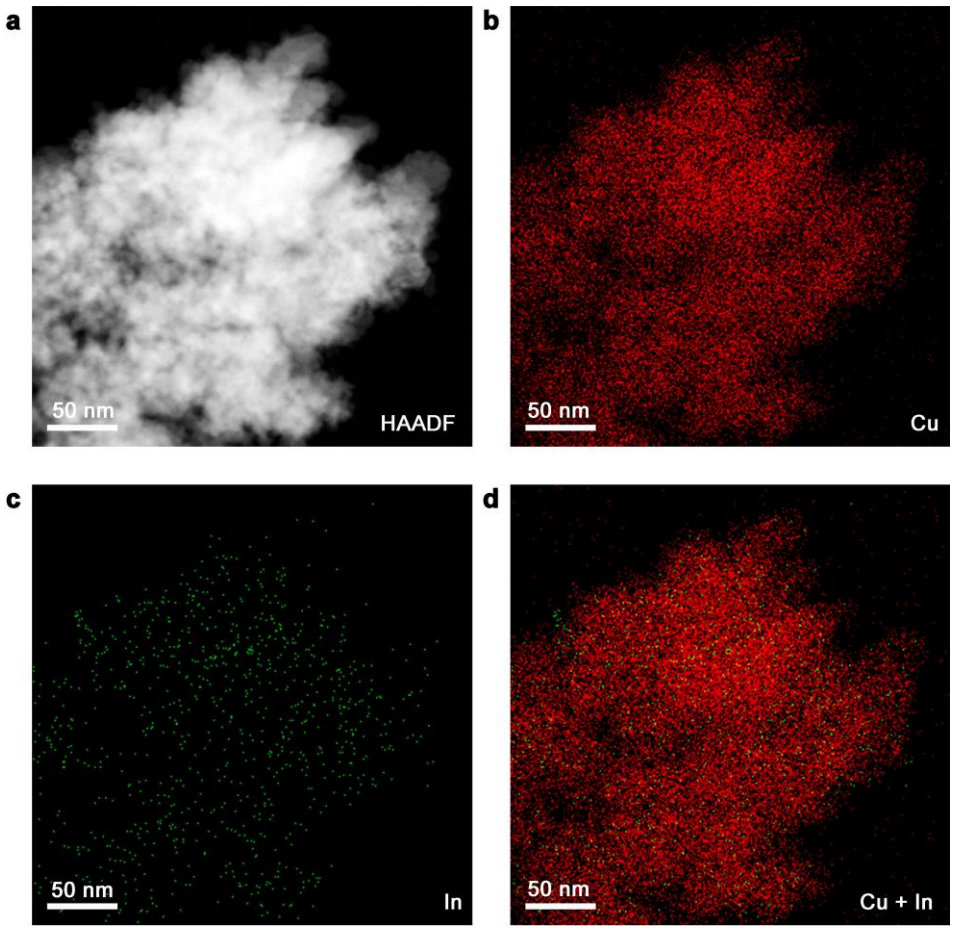

Supplementary Fig. 31 | STEM-EDS mapping of In_1Cu SAA catalyst. The images showed the atomic dispersion of In in the Cu matrix.

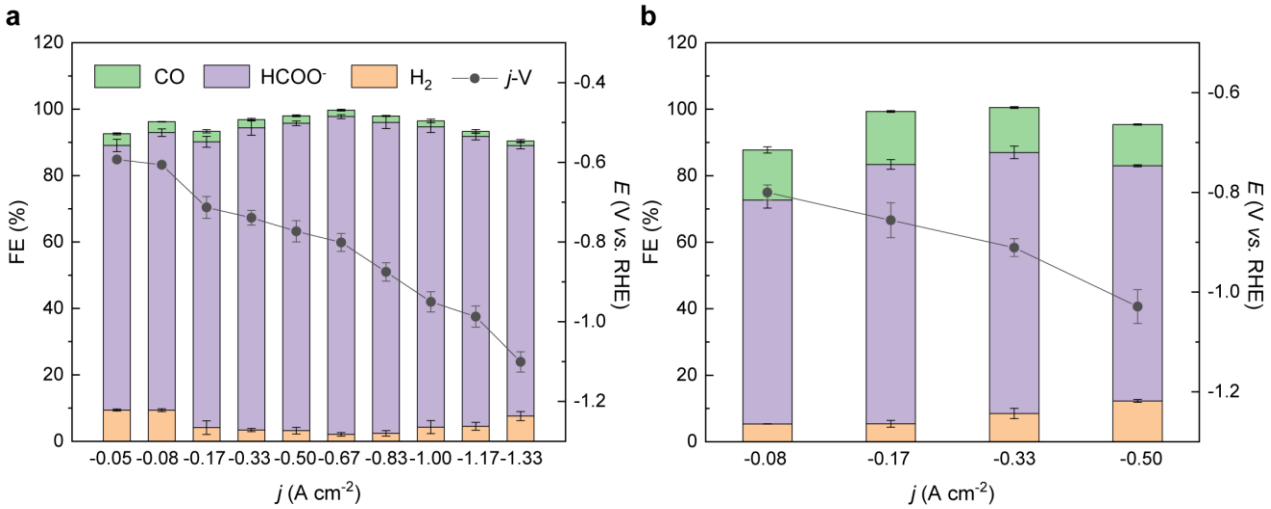

Supplementary Fig. 32 | CO_2RR performance of Bi_1Cu SAA catalyst (a) and In_1Cu SAA catalyst (b) in a flow cell. FEs of all CO_2 reduction products at different current densities and the corresponding *j*-V curve of catalysts. The error bars correspond to the standard deviation of three independent measurements. The values of potential were manually compensated according to the measured electrolyte resistance and corrected to RHE scale. The remarkable $HCOO^-$ yield proved the universal effect of single atom alloying strategy.

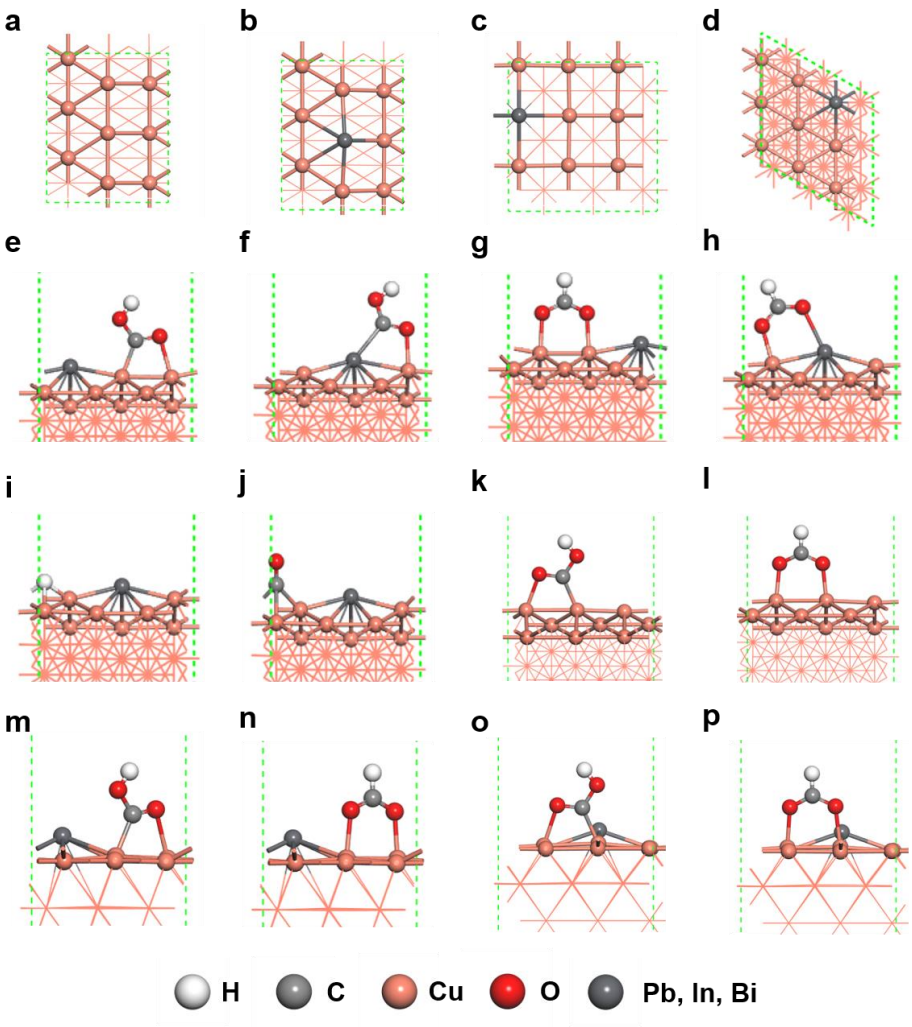

Supplementary Fig. 33 | Surface structures. a-p, The surface structures of Cu(211) (**a**), $M_1Cu(211)$ (**b**), $M_1Cu(100)$ (**c**), and $M_1Cu(111)$ (M = Pb, In, Bi) (**d**). The adsorption states of COOH* on $M_1Cu(211)_{Cu\text{-}Cu}$ (**e**), $M_1Cu(211)_{M\text{-}Cu}$ (**f**), Cu(211) (**k**), $M_1Cu(111)_{Cu\text{-}Cu}$ (**m**), and $M_1Cu(100)_{Cu\text{-}Cu}$ (**o**). The adsorption states of HCOO* on $M_1Cu(211)_{Cu\text{-}Cu}$ (**g**), $M_1Cu(211)_{M\text{-}Cu}$ (**h**), Cu(211) (**l**), $M_1Cu(111)_{Cu\text{-}Cu}$ (**n**), and $M_1Cu(100)_{Cu\text{-}Cu}$ (**p**). The adsorption states of H* on $M_1Cu(211)_{Cu\text{-}Cu}$ (**i**). The adsorption states of CO* on $M_1Cu(211)_{Cu\text{-}Cu}$ (**j**).

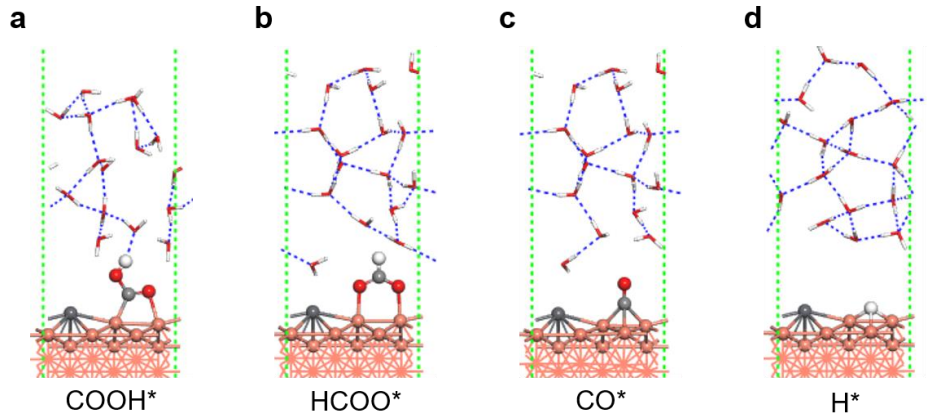

Supplementary Fig. 34 | Explicit models for solvation effect on adsorbed COOH*, HCOO*, CO* and H*. 16 H_2O molecules were applied in one unit cell, establishing the water layer over 12 Å.

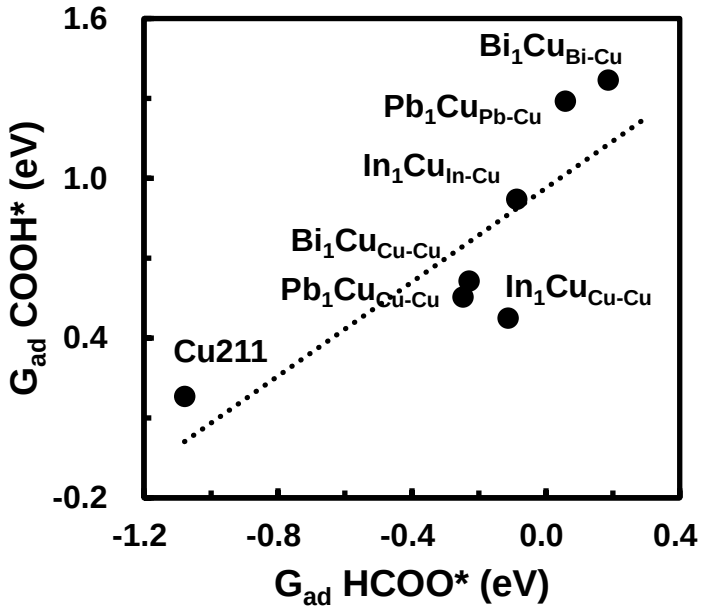

Supplementary Fig. 35 | The linear correlation between the adsorption free energies of COOH* and HCOO*, for establishing 1D reaction phase diagram.

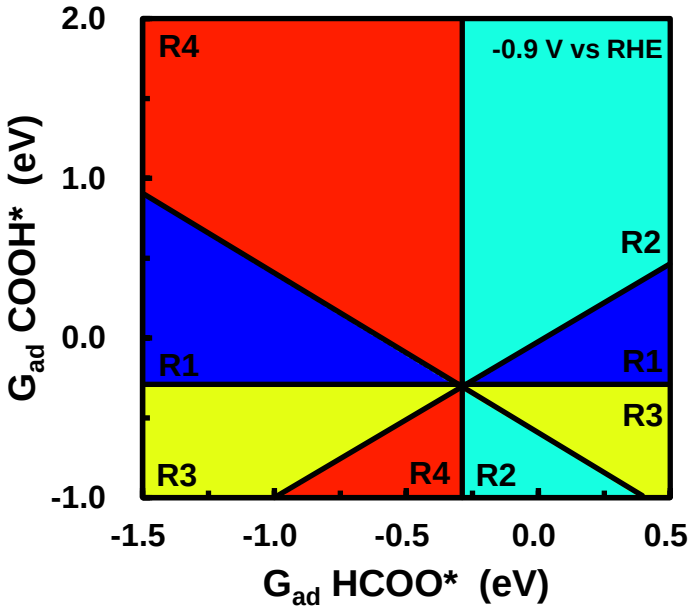

Supplementary Fig. 36 | G_{RPD}-limiting steps obtained based on the scheme of reaction phase diagram.

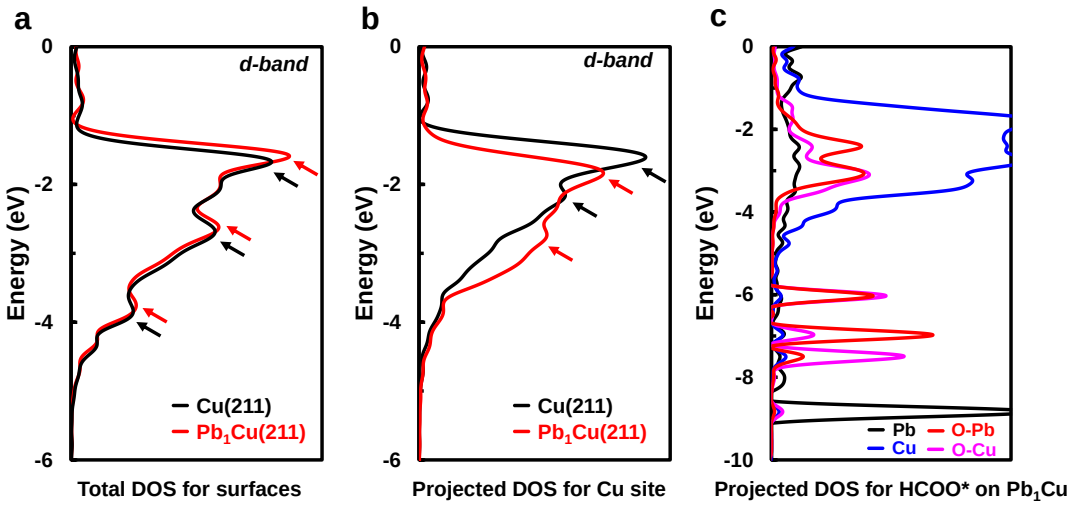

Supplementary Fig. 37 | The density of state for d-orbitals on Cu and Pb_1Cu surface. a, A weaker binding ability can be expected as a general trend due to the higher energy level of the total d-band on Pb_1Cu rather than Cu. **b**, The lower energy level of the project d-band for Cu site on Pb_1Cu indicates a stronger binding with the surface, also revealing a weaker binding ability for additional adsorbates compared with that on Cu, which is consistent with the result from total DOS analysis. **c**, The higher energy level and less overlap of PDOS between Pb and O (binding with Pb) indicates a stronger binding ability compared with that for Pb.

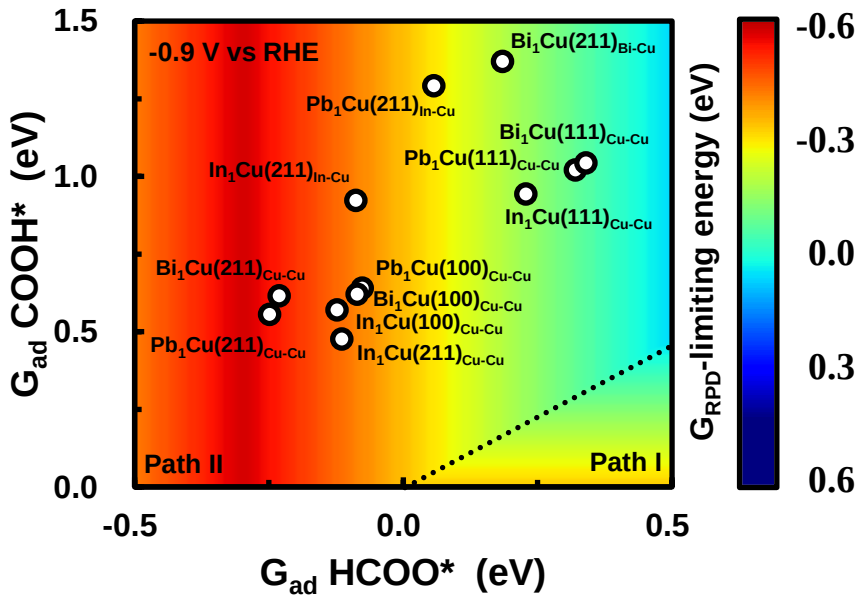

Supplementary Fig. 38 | The two-dimensional (2D) reaction phase diagram. The 2D RPD for CO_2RR producing formic acid with independent descriptors of the adsorption free energies of HCOO* and COOH* over various sites over (211), (111) and (100) facets. Two different adsorption conditions were studied for the adsorption of HCOO* and COOH*, including $M_1Cu_{M\text{-}Cu}$ (M = Pb, In, Bi; the adsorbate was bonded with M site and Cu site on the surface, the Cu site is the first neighbour of M site) and $M_1Cu_{Cu\text{-}Cu}$ (M = Pb, In, Bi; the adsorbate was bonded with two Cu sites on the surface, one of the Cu site is the first neighbour of M site) (**Supplementary Fig. 33**).

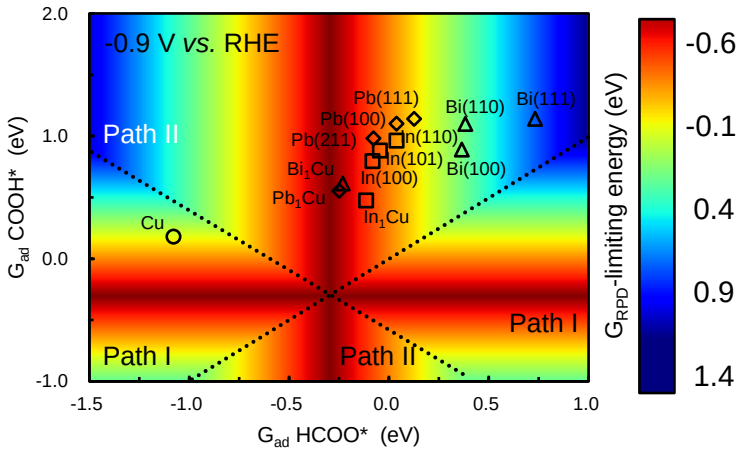

Supplementary Fig. 39 | The two-dimensional (2D) reaction phase diagram for the comparison of activities on Cu alloys and Pb, In, Bi pure metals.

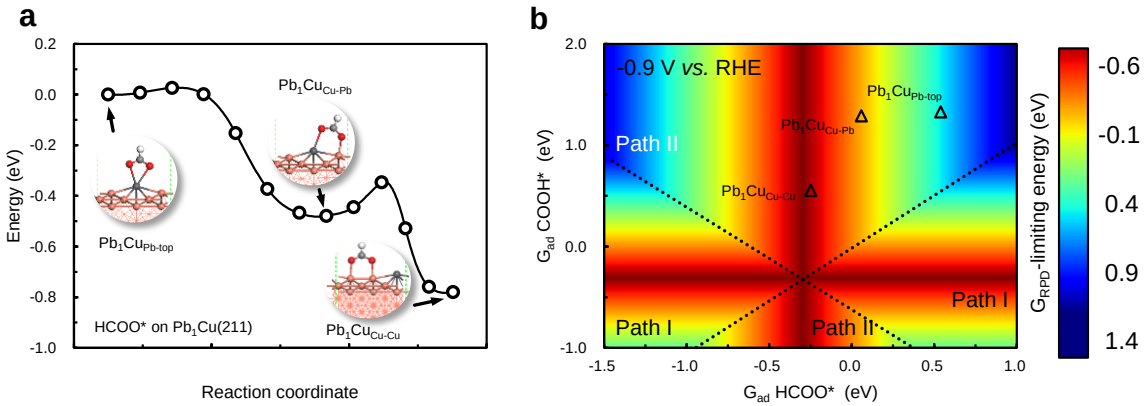

Supplementary Fig. 40 | A comparison of different sites on Pb_1Cu. a, The energy change in the process of site transfer for HCOO* from Pb-top site to Pb-Cu and Cu-Cu site on Pb_1Cu. **b**, The two-dimensional (2D) reaction phase diagram showing activity of CO_2RR producing formate for different active site on Pb_1Cu.

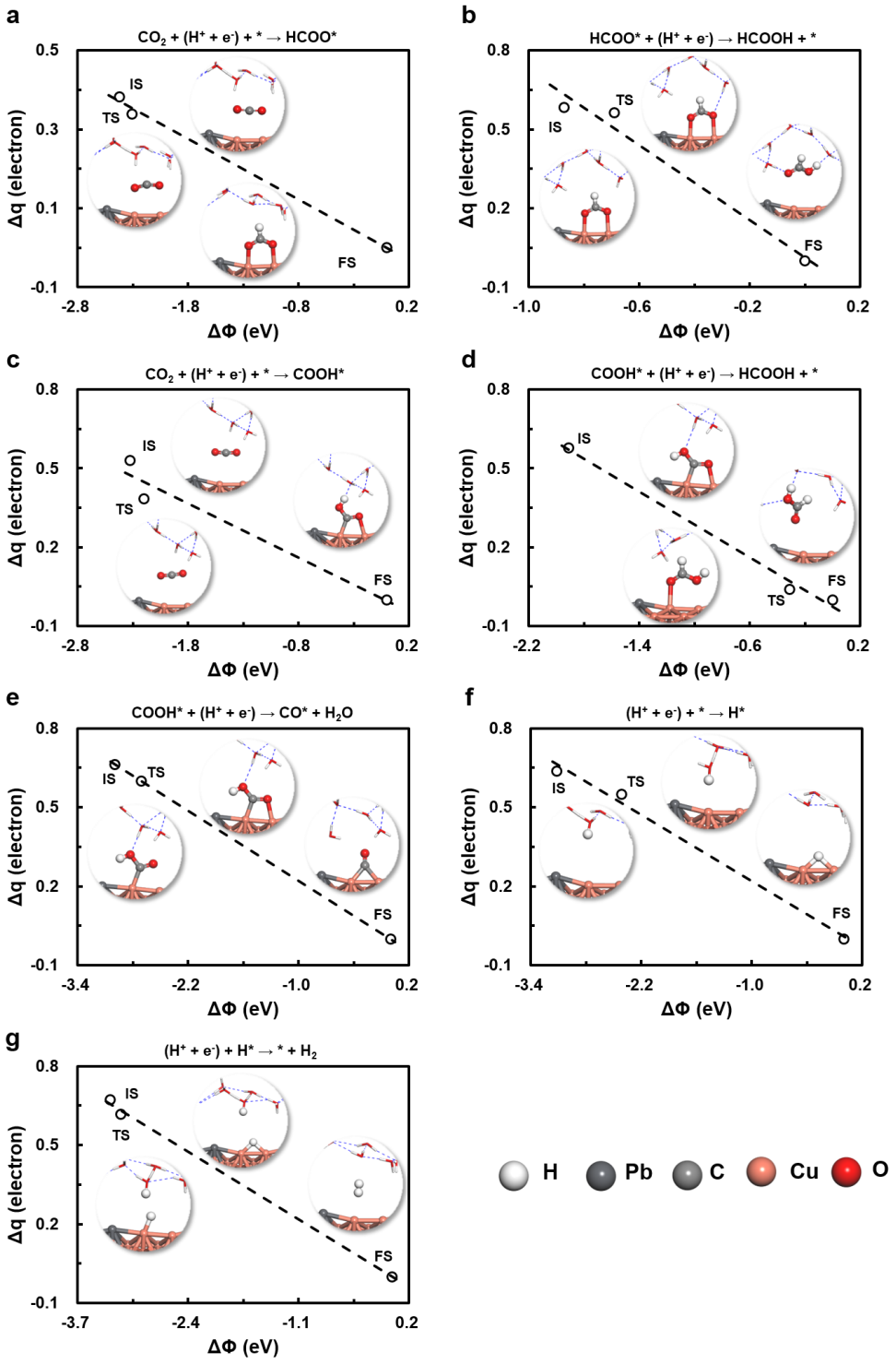

Supplementary Fig. 41 | The scheme of 'charge-extrapolation'. The linear correlation between the amount of electron transfer (Δq) and the relative work function of the system ($\Delta\Phi$) at initial, transition and final states for all studied electrochemical steps. The amount of electron transfer and the relative work function of the system at the final state were applied as a reference.

Supplementary Table 1 | EXAFS fitting datas at the Pb L_{III}-edge for Pb_1Cu（S_0^2=0.834）

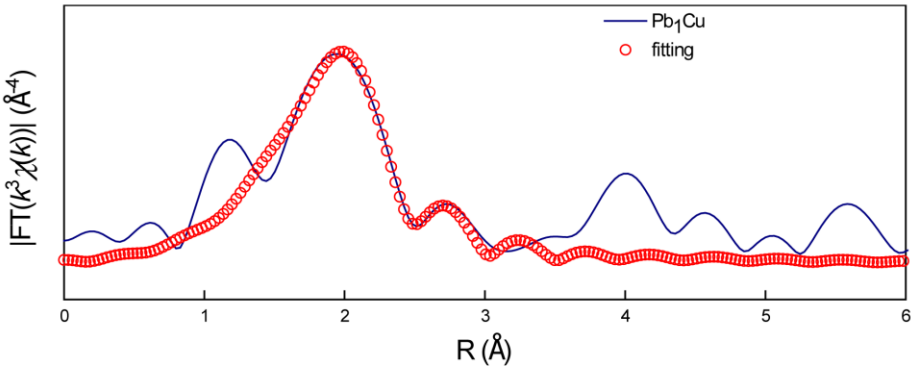

Sample	Shell	N^a	R(Å)^b	σ^2(Å^2)^c	ΔE_0(eV)^d	R factor
PbCu	Pb-O	4.9	2.43	0.0067	-9.6	0.0011
	Pb-Cu	1.6	2.99	0.0131		

$^a N$: coordination numbers; $^b R$: bond distance; $^c \sigma^2$: Debye-Waller factors; $^d \Delta E_0$: the inner potential correction. R factor: goodness of fit. S_0^2 was set to 0.834, according to the experimental EXAFS fit of Pb foil reference by fixing CN as the known crystallographic value.

Supplementary Table 2 | The original measurement data for Figure 2a and b. The data was calculated based on the average values from three independent Pb_1Cu catalysts.

iR-uncorrected potential (V *vs.* Ag/AgCl)	FE $_{H2}$(%)	FE_{HCOO-}(%)	FE_{CO}(%)	J (mA cm^{-2})	J_{HCOO-} (mA cm^{-2})
-1.62	12.40895	78.4334	0.72933	-50	-39
-1.83	9.17251	85.96871	0.6975	-83	-71
-2.08	7.52194	87.60774	0.607	-167	-146
-2.21	6.59228	89.39997	0.28696	-333	-298
-2.49	5.67959	92.30759	0.26918	-500	-462
-2.76	4.86756	95.00769	0.21735	-667	-634
-2.97	4.3055	96.11707	0.35559	-833	-801
-3.25	4.79143	93.75612	0.40856	-1000	-938
-3.46	5.32742	92.0871	0.39881	-1167	-1075
-3.58	5.40841	85.86536	0.34904	-1333	-1145
-3.77	8.46748	80.18862	0.30659	-1500	-1203

Supplementary Table 3 | Comparison of CO_2 RR performance merits in a H-cell.

Catalyst	FE(%)	Current density (mA cm^{-2})	Voltage (V *vs.* RHE)	Reference
Pb_1Cu	95.74	-6.4	-0.72	This work
	91.8	-12	-0.78	
	86.2	-19.4	-0.83	
Pd-B/C	70	-3.98	-0.5	*J. Am. Chem. Soc. 140, 2880-2889 (2018)*
BiNS	81.5	-24	-1.06	*Nat. Commun. 9, 1320 (2018)*
BiNSs	99	-3	-0.58	*Nat. Commun. 11,1088 (2020)*
2D-Bi	99	-17.3	-0.79	*Nat. Energy. 4, 776 (2019)*
$CuSn_3$	95	-31	-0.5	*Nat. Catal. 2, 55 (2019)*
Cu-CTAB	82.3	-2.48	−0.5	*ACS Catal. 10, 16, 9271-9275(2020)*
$PdAg_2$	90	-3.6	-0.35	*Adv. Mater. 32, 2000992 (2020)*
Bi_2O_3-NG QDs	~100	-17.5	-0.9	*Angew. Chem. Int. Ed. 57,12790 -12794 (2018)*
InO_x NRs	90.2	-7.8	-0.8	*Angew. Chem. Int. Ed. 58, 5609 -5613 (2019)*
SnO_2 QWs	87.3	-18.1	-0.82	*Angew. Chem. Int .Ed. 58, 8499 -8503 (2019)*
Bi_2O_3@C-800	92	-12.4	-0.9	*Angew. Chem. Int. Ed. 59, 10807-10813 (2020)*
Bi_2O_3 NSs@MCCM	93.8	-17.7	-1.256	*Angew. Chem. Int.Ed. 58,13828 -13833 (2019)*
Bi-300	~100	-8	-0.7	*Angew. Chem. Int. Ed.*

				59,20112-20119 (2020)
NiSn-APC	86.1	-20.8	-0.82	*Angew. Chem. Int. Ed. 60,7382-7388 (2021)*

Supplementary Table 4 | The comparison about parameters of pure formic acid electrosynthesis in solid electrolyzer between this work and previous reports.

electrocatalysts	formic acid FE (%)	current density (mA cm^{-2})	operating time (h)	ref.
Pb_1Cu	94	-133	/	This work
	80	-300	/	
	avg. 85	-100	180	
2D-Bi	~90	-100	/	*Nat. Energy 4, 776-785 (2019)*
	~80	-200		
	avg. 80	-30	100	
nBuLi-Bi	~93	-100	/	*Nat. Commun. 11, 3633 (2020)*
	~85	~-280	/	
	avg. 60	-30	100	

Supplementary Table 5 | Free energy corrections for gas molecules and adsorbates.

	Free energy corrections (eV)
H_2	-0.04
H_2O	-0.01
CO	-0.39
CO_2	-0.27
HCOOH	0.25
COOH*	0.52
HCOO*	0.50
CO*	0.12
H*	0.17

Supplementary Table 6 | The solvation effect based on explicit model and implicit model.

	Adsorption energy (E_{ad})			
	COOH*	HCOO*	CO*	H*
Without solvent effect	-0.17	-1.07	-0.51	-0.09
With solvent effect		Explicit model		
No.1	-0.18	-1.24	-0.53	-0.11
No.2	-0.29	-1.14	-0.58	-0.10
No.3	-0.48	-1.05	-0.58	-0.10
No.4	-0.37	-1.13	-0.55	-0.10
No.5	-0.43	-1.09	-0.51	-0.10
E_{ad} (Average)	-0.35	-1.13	-0.55	-0.10
		Implicit model		
E_{ad}	-0.33	-1.14	-0.54	-0.09
	Solvation effect (ΔE_{ad})			
Explicit model	-0.18	-0.06	-0.04	-0.01
Implicit model	-0.16	-0.07	-0.03	-0.00

Supplementary Table 7 | Potential dependent energy change for activation barriers based on the capacitor model[#].

	φ_1	φ_2	$E_2(\varphi_2) - E_1(\varphi_1)$	q_1	q_2	$E_2(\varphi_1) - E_1(\varphi_1)$	$E_2(\varphi_2) - E_1(\varphi_2)$
R1	-2.59	-1.88	0.11	0.53	0.38	0.05	0.16
R2	-2.50	-2.21	0.32	0.38	0.34	0.31	0.32
R3	-1.84	-0.13	-1.64	0.58	0.04	-2.10	-1.18
R4	-0.82	-0.80	-0.01	0.59	0.57	-0.01	-0.01
R5	-2.99	-2.71	-0.17	0.66	0.60	-0.17	-0.16
R7	-3.03	-2.61	0.59	0.64	0.55	0.57	0.61
R8	-3.39	-3.11	0.91	0.67	0.62	0.90	0.92

[#] R1 – R8 represent to the electrochemical steps, see discussions above. State 1 and 2 refer to the initial and transition states.

Supplementary Table 8 | Potential dependent energy change for reaction energies based on the capacitor model[#].

	φ_1	φ_2	$E_2(\varphi_2) - E_1(\varphi_1)$	q_1	q_2	$E_2(\varphi_1) - E_1(\varphi_1)$	$E_2(\varphi_2) - E_1(\varphi_2)$
R1	-2.59	0.00	-1.20	0.64	0.00	-2.95	-1.89
R2	-2.50	0.00	-2.18	0.67	0.00	-1.82	-1.33
R3	-1.84	0.00	-2.42	0.53	0.00	-3.01	-1.03
R4	-0.82	0.00	-1.57	0.38	0.00	-1.80	0.13
R5	-2.99	0.00	-2.02	0.58	0.00	-1.75	0.53
R7	-3.03	0.00	-0.84	0.59	0.00	-1.89	-0.51
R8	-3.39	0.00	-0.61	0.66	0.00	-2.66	-1.70

[#] R1-R8 represent to the electrochemical steps, see discussions above. State 1 and 2 refer to the initial and final states.

Supplementary Table 9 | The calculated rate of CO_2RR producing formic acid and CO with HER based on microkinetic modeling.

Elementary steps	Rate (TOF)
$CO_2 + (H^+ + e^-) + * \rightarrow COOH*$	6.08×10^{-3}
$CO_2 + (H^+ + e^-) + * \rightarrow HCOO*$	1.92×10^{-1}
$COOH* + (H^+ + e^-) \rightarrow HCOOH + *$	3.04×10^{-3}
$HCOO* + (H^+ + e^-) \rightarrow HCOOH + *$	1.92×10^{-1}
$COOH* + (H^+ + e^-) \rightarrow CO* + H_2O$	3.04×10^{-3}
$CO* \rightarrow CO + *$	3.04×10^{-3}
$(H^+ + e^-) + * \rightarrow H*$	4.35×10^{-4}
$(H^+ + e^-) + H* \rightarrow H_2 + *$	4.35×10^{-4}

References

1 Kresse, G. & Furthmüller, J. Efficiency of ab-initio total energy calculations for metals and semiconductors using a plane-wave basis set. *Comput. Mater. Sci.* **6**, 15-50 (1996).

2 Kresse, G. & Hafner, J. Ab initio molecular-dynamics simulation of the liquid-metal–amorphous-semiconductor transition in germanium. *Phys. Rev. B* **49**, 14251-14269 (1994).

3 Zhang, Y. & Yang, W. Comment on "Generalized Gradient Approximation Made Simple". *Phys. Rev. Lett.* **80**, 890-890 (1998).

4 Blöchl, P. E., Jepsen, O. & Andersen, O. K. Improved tetrahedron method for Brillouin-zone integrations. *Phys. Rev. B* **49**, 16223-16233 (1994).

5 Kresse, G. & Joubert, D. From ultrasoft pseudopotentials to the projector augmented-wave method. *Phys. Rev. B* **59**, 1758-1775 (1999).

6 Cao, X. M., Burch, R., Hardacre, C. & Hu, P. An understanding of chemoselective hydrogenation on crotonaldehyde over Pt(1 1 1) in the free energy landscape: The microkinetics study based on first-principles calculations. *Catal. Today* **165**, 71-79 (2011).

7 Guo, C., Fu, X. & Xiao, J. Theoretical Insights on the Synergy and Competition between Thermochemical and Electrochemical Steps in Oxygen Electroreduction. *J. Phys. Chem. C* **47**, 25796–25804 (2020).

8 Xu, H., Cheng, D., Cao, D. & Zeng, X. C. A universal principle for a rational design of single-atom electrocatalysts. *Nat. Catal.* **1**, 339-348 (2018).

9 Cheng, T. *et al.* Mechanism and kinetics of the electrocatalytic reaction responsible for the high cost of hydrogen fuel cells. *Phys. Chem. Chem. Phys.* **19**, 2666-2673 (2017).

10 Mathew, K., Sundararaman, R., Letchworth-Weaver, K., Arias, T. A. & Hennig, R. G. Implicit solvation model for density-functional study of nanocrystal surfaces and reaction pathways. *J. Chem. Phys.* **140**, 084106 (2014).

11 Nørskov, J. K. *et al.* Origin of the Overpotential for Oxygen Reduction at a Fuel-Cell Cathode. *J. Phys. Chem. B* **108**, 17886-17892 (2004).

12 Chan, K. & Norskov, J. K. Potential Dependence of Electrochemical Barriers from ab Initio Calculations. *J. Phys. Chem. Lett.* **7**, 1686-1690 (2016).

13 Henkelman, G., Uberuaga, B. P. & Jónsson, H. A climbing image nudged elastic band method for finding saddle points and minimum energy paths. *J. Chem. Phys.* **113**, 9901-9904 (2000).

14 Li, H., Guo, C., Fu, Q. & Xiao, J. Toward Fundamentals of Confined Electrocatalysis in Nanoscale Reactors. *J. Phys. Chem. Lett.* **10**, 533-539 (2019).

15 Guo, C., Mao, Y., Yao, Z., Chen, J. & Hu, P. Examination of the key issues in microkinetics: CO oxidation on Rh(1 1 1). *J. Catal.* **379**, 52-59 (2019).

16 Chen, J.-F., Mao, Y., Wang, H.-F. & Hu, P. Reversibility Iteration Method to Understand Reaction Networks and to Solve Micro-Kinetics in Heterogeneous Catalysis. *ACS Catal.* **6**, 7078-7087 (2016).